This is the Pre-Published Version.
This document is the Accepted Manuscript version of a Published Work that appeared in final form in Environmental Science & Technology, copyright © 2023 American Chemical Society after peer review and technical editing by the publisher. To access the final edited and published work see https://dx.doi.org/10.1021/acs.est.2c09252.

Molecular characterization of oxygenated organic molecules and their dominating roles in particle growth in Hong Kong

*Penggang Zheng [1,2], Yi Chen [1,2], Zhe Wang [1, *], Yuliang Liu [3], Wei Pu [2], Chuan Yu [2], Men Xia [2], Yang Xu [1], Jia Guo [4], Yishuo Guo [5], Linhui Tian [6], Xiaohui Qiao [7], Dan Dan Huang [8], Chao Yan [3,9], Wei Nie [3], Douglas R. Worsnop [9, 10], Shuncheng Lee [2], Tao Wang [2]*

[1] Division of Environment and Sustainability, The Hong Kong University of Science and Technology, Hong Kong SAR 999077, China

[2] Department of Civil and Environmental Engineering, The Hong Kong Polytechnic University, Hong Kong SAR 999077, China

[3] Joint International Research Laboratory of Atmospheric and Earth System Research, School of Atmospheric Sciences, Nanjing University, Nanjing 210023, China

[4] Environmental Central Facility, The Hong Kong University of Science and Technology, Hong Kong SAR 999077, China

[5] Aerosol and Haze Laboratory, Beijing Advanced Innovation Center for Soft Matter Science and Engineering, Beijing University of Chemical Technology, Beijing 100084, China

[6] Department of Civil and Environmental Engineering, Faculty of Science and Technology, University of Macau, Taipa, Macau 999078, China.

[7] State Key Joint Laboratory of Environment Simulation and Pollution Control, School of Environment, Tsinghua University, Beijing 100084, China

[8] State Environmental Protection Key Laboratory of Formation and Prevention of Urban Air Pollution Complex, Shanghai Academy of Environmental Sciences, Shanghai 200233, China

[9] Institute for Atmospheric and Earth System Research / Physics, Faculty of Science, University of Helsinki 00014, Finland

[10] Aerodyne Research Inc., Billerica, MA 01821, USA.

Abstract

Oxygenated organic molecules (OOMs) are critical intermediates linking volatile organic compounds (VOCs) oxidation and secondary organic aerosol (SOA) formation. Yet the understanding of OOM components, formation mechanism and impacts are still limited, especially for urbanized region with a cocktail of anthropogenic emissions. Herein, ambient measurements of OOMs were conducted at a regional background site in South China in 2018. The molecular characteristics of OOMs revealed dominant nitrogen containing products, and the influences of different factors on OOMs composition and oxidation state were elucidated. Positive matrix factorization (PMF) analysis resolved the complex OOM species to factors featured with fingerprint species from different oxidation pathways. A new method was developed to identify the key functional groups of OOMs, and successfully classified the majority species into carbonyls (8%), hydroperoxides (7%), nitrates (17%), peroxyl nitrates (10%), di-nitrates (13%), aromatic ring-retaining species (6%) and terpenes (7%). The volatility estimation of OOMs was improved based on their identified functional groups and was used to simulate the aerosol growth process contributed by the condensation of those low-volatile OOMs. The results demonstrate the predominant role of OOMs in contributing sub-100nm particle growth and SOA formation, and highlight the importance of di-nitrates and anthropogenic products from multistep oxidation.

Keywords: *Oxygenated organic molecules (OOMs); Positive matrix factorization (PMF); Categorization scheme; Multifunctional oxidation products; Nanoparticle growth; Chemical ionization mass spectrometer (CIMS)*

Synopsis

A new categorization scheme is developed to characterize the oxygenated organic molecules observed in subtropical Hong Kong, revealing the dominant roles of the anthropogenic low-volatile organic vapors in particle growth.

Graphic for Table of Contents (TOC)

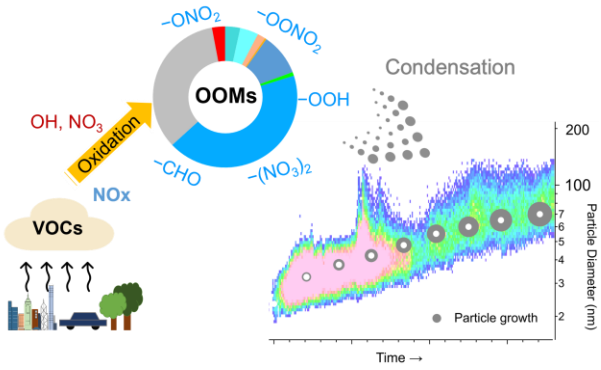

1. Introduction

The atmospheric oxidation of volatile organic compounds (VOCs) is the critical tropospheric process in forming ozone (O_3) and secondary organic aerosols (SOA), adversely affecting the human health and the climate[1, 2]. Substantial research efforts have been made to understand the key VOC precursors and oxidation mechanisms contributing to SOA formation[3-5], and recent research advances were benefited from the development of high-resolution mass spectrometer (MS) techniques to detect low-volatile highly oxygenated organic molecules (HOMs)[6, 7]. Field and laboratory studies have revealed large amounts of HOMs, as the key intermediates in the oxidation process of biogenic VOCs, can condense irreversibly to contribute SOA formation[7-11]. More recently, oxygenated organic molecules (OOMs) with some less oxygenated species from anthropogenic VOCs were detected in polluted urban regions with abundant NOx, and also significantly contribute to SOA formation[12-15]. In addition, studies also suggested that that OOMs can be involved in the initial clustering process of new particle formation [16, 17], and play important roles in the subsequent growth of particles by condensation process[18].

The OOMs (including HOMs) formation mechanism has been probed in some field and laboratory studies. Autoxidation of peroxy radicals (RO_2) has been recognized as the key step in the OOMs formation from various precursors[7]. Ehn et al., revealed the nocturnal HOM formation in the ozonolysis of α-pinene at a boreal forest site[8, 19, 20]. Guo et al. investigated the HOMs formation from the reaction of limonene with nitrate radical[21]. Wennberg et al.[22, 23] summarized the isoprene oxidation process and reported the major production of $C_{4\text{-}5}$-OOMs in the atmosphere. The oxidation of aromatics by OH radical have also been investigated in laboratory and theoretical studies[24-31], and both the OH radical addition and H-abstraction processes are proved to be important in the oxidation process, producing ring-opening and ring-retaining OOMs, respectively.

Wang et al.[32] measured the combustion exhaust of alkane in the air and found effective autoxidation of C_{6-10} alkanes in producing OOMs and contributing to urban organic aerosols. Despite increasing research efforts in OOMs formation mechanisms, most previous studies concentrated on a simple oxidation system in the chamber or clean environment. Few direct observations exist in urban atmosphere with a cocktail of complex anthropogenic pollutants, and the OOMs speciation, formation mechanism and impacts on SOA formation are still vague in the polluted urban environments. Recent field studies in several Chinese megacities revealed that abundant OOMs could be produced from anthropogenic VOCs, and can contribute 38-71% of observed SOA formation[14, 15, 33] and promote the growth of newly formed nano-particles[13]. These results highlight the crucial roles of OOMs connecting the VOC oxidation and SOA formation in different environments and worth of further in-depth study.

In addition to the precursor types and oxidants, temperature and NOx are also two essential factors affecting the OOMs formation and composition. Frege et al.[34] found higher signals and more oxidized OOMs formed under higher temperature condition in the ozonolysis of α-pinene, suggesting the acceleration role of temperature on RO_2 autoxidation process. Stolzenburg et al.[35] reported that although more oxidized OOMs were produced under high temperature condition, the simultaneously increased volatility of OOMs could offset such enhancement in condensation to some extent. A recent comparison on OOMs levels measured worldwide revealed the clear seasonal pattern of OOMs and that elevated solar radiation along with temperature promoted the OOMs formation[36]. In urban environments, high level of NO_x could outcompete the autoxidation propagation reactions, affect termination pathway of RO_2 radicals and also change the atmospheric oxidants (e.g., affect OH/HO_2 radicals levels and produce NO_3 radicals). It will eventually influence the OOMs products types, distributions, and contributions to SOA[7, 37-41]. Recent field

studies highlighted such suppression effects of NOx on the oxidation degree of OOMs in urban atmosphere in East China.[12, 42] Moreover, though the molecular features of OOMs in terms of element numbers has been explored in previous studies [12, 14, 36], limited information is available on their multifunctional groups[24, 30, 43, 44], which hinder the complete understanding of their atmospheric fates and impacts.

To address research needs expressed above, comprehensive field measurements of OOMs were conducted at a coastal background site in Hong Kong during photochemical seasons in 2018. The molecular information of the measured OOMs were characterized in detail, and the impacts of different environmental factors on OOMs products distribution were investigated. Based on the positive matrix factorization (PMF) analysis, the key oxidation products and formation pathways were investigated, and a new classification scheme was developed to better categorize the complex OOMs molecules from different precursors and termination reactions. Applying the new approach, the volatility and OSc of measured OOMs was estimated and the size-dependent contribution of the OOMs on the particle growth rate was evaluated.

2. Methodology

2.1 Field measurement and instrumentation

The field campaign was conducted at a coastal background site in Hong Kong from the autumn to winter (from 20th September to 8th October, and 1st November to 18th December) of 2018. The measurement site is located at the Cape D'Aguilar Supersite Air Quality Monitoring Station (CDSS, 22.22°N, 114.25°E) of Hong Kong Environmental Protection Department (HKEPD), and stands on a cliff surrounded by the sea on three sides. The supersite is around 10 km away from the metropolitan area, and usually intercepts the aged urban plumes from Hong Kong and continental

outflows from South and East China. More detailed description of the monitoring site can be found in our previous work[14, 45].

A nitrate-based chemical ionization time-of-flight mass spectrometer (NO_3-CI-ToF-MS) was deployed to measure the ambient OOMs and sulfuric acids. Briefly, ambient air at a flow rate of 10 LPM was pulled into the chemical ionization chamber, where the OOMs were ionized by nitrate clusters and then measured by mass spectrometer. With the high mass spectral resolution (5200 at 200Th), more than 1300 molecular peaks were identified using a newly developed approach based on binned positive matrix factorization (binPMF)[46]. The CI-ToF-MS was calibrated with sulfuric acid, the calibration factor of which was also applied to the measured OOMs, with the mass transmission corrections[47]. This is the preferred method in the present to calibrate the numerous and structure-unclear OOMs detected by nitrate-CI-ToF-MS[48]. Details of the instrument setup, calibration and transmission methodology were described in SI and our previous studies[7, 47]. During the campaigns, NO, NOx, O_3, N_2O_5, particle size distribution, and meteorology information, were also concurrently measured at the site. Some un-measured species, including OH, HO_2, NO_3 radicals were simulated using an observation-based photochemical model built on Master Chemical Mechanism (MCM v3.3.1), and detailed information can be found in SI and our previous work[45].

2.2 Data analysis

The identification of OOMs molecular information and formation mechanism with ambient data has been very challenging. PMF is a powerful receptor model and has been widely used to extract ambient pollutants with unclear formation pathways and profiles[49]. The model mathematically distributes the measured dataset to several constant profiles with the time-dependent variation, and potentially separate the OOMs with different structures and formation pathways. Here, the PMF2

144 developed by Paatore et al.[50, 51] were used and a total of 967 concerned OOM species were input
145 into the model. The signal error was estimated following Yan et al.'s method[44]. Solutions ranging
146 from 3 to 20 were tested in the model. 6 factors solution were eventually selected as the optimized
147 source solution based on the Q/Qexp and the up-to-date knowledge of gas-phase oxidation and
148 OOMs formation. Details about the PMF analysis and solution diagnostics can be found in the SI.

149 The carbon oxidation state (OS_c) and volatility are two important metrics to represent the chemical
150 and physical properties of OOMs. The OSc of the measured OOMs was calculated based on the
151 identified functional groups. The volatility of different OOMs were also estimated using
152 parameterization method proposed by Donahue et al[52] and also the functional groups contribution
153 method (simplified p_L^o prediction method, SIMPOL.1) developed by Pankow et al.[53] More
154 detailed information is provided in the SI. The condensation of low-volatile OOMs and the
155 equilibrium partitioning of semi-VOCs (SVOC) are two main driving forces that promote the
156 particles growth. Here, we used the aerosol growth model and partitioning equilibrium function to
157 quantify these two processes, respectively[54, 55]. The growth rate through condensation is obtained
158 by,

$$GR = \frac{2}{\pi \rho_p d_p^2} \frac{dm_p}{dt} = \frac{2}{\pi \rho_p d_p^2} \cdot \sigma_p \cdot k_p \cdot F_p \qquad \text{Eq1}$$

159 where d_p is the particle diameter, ρ_p is the particle density and d_{mp}/d_t is the mass flux onto the
160 particle. The mass flux can be further calculated with the aerosol growth model, with σ_p the
161 particle-vapor collision cross-section, k_p the deposition rate of vapors at the surface and F_p the
162 driving force. The contribution of SVOC through the gas-particle partitioning was estimated by
163 the equilibrium function equation, as described in the SI.

3. Results and discussion

3.1 Overview

3.1.1 Molecular characteristics of OOMs

A total of 967 OOMs species with m/z ranging from 50 to 400 were identified and analyzed in the present field study. Figure 1a shows the mass defect (MD) plot of measured compounds, which is most featured with a bulk of upward inclined molecule bands (shown as black arrows in **Figure 1**a), representing a series of homologs that differed by -CH_2. Then, the major OOMs species could be classified into several homologous series, i.e., $C_nH_{2n-4}O_4$, $C_nH_{2n-2}O_5$, $C_nH_{2n-2}NO_6$, $C_nH_{2n-2}NO_7$, $C_nH_{2n-2}N_2O_8$, and $C_nH_{2n-1}N_3O_{10}$ (n ranges from 4 to 11). Most of OOMs observed in this campaign contained zero to three N atoms (**Figure 1**a), and the non-nitrogen (CHO), one nitrogen (CHON), two nitrogen ($CHON_2$) and three nitrogen ($CHON_3$) species accounted for 35.2%, 44.5%, 18.0%, 2.2% of total measured OOMs, respectively (**Figure 1**a). The proportion of nitrogen-containing OOMs in Hong Kong was similar to other urban measurements with abundant anthropogenic VOCs and NOx [12, 13], and was much higher than the results at rural forest site in Hyytiälä[56], where predominant biogenic VOC and low NOx level (daytime median 0.30 ppbv)[57] contributed more than 50% non-nitrogen OOMs. The contribution of autoxidation in OOMs formation can also be observed from the sequential O_2 addition in the measured OOMs formula with downward inclined molecule bands (shown as blue arrow) in **Figure 1**a.

The OSc of measured OOMs species as a function of carbon numbers is shown in **Figure 1**b. A clear belt from the lower-left corner to the upper-right corner can be seen, and similar pattern was observed in the oxidation experiments of α-pinene and isoprene, representing the life course of atmospheric VOCs oxidation ultimately towards CO_2[58]. Throughout the entire campaign, the OSc

of OOMs basically ranged from -2 to 2 with a campaign average of -0.148, which is comparable to observed values of -0.043 and -0.68 for OOMs in a forest site in Alabama and an urban site in Shanghai, respectively. The concentration weighted mean OSc increased with the decrease of carbon number, which is consistent with the negative relationship of OSc and nC in the definition equation. Compounds with higher OSc (>2) were not observed presumably because species with more than 3 adjacent carbonyl groups were thermodynamically or photochemically unstable, and would rapidly decompose to smaller nC species[58]. Compounds with lower OSc (<-2) species were insensitive towards the current equipment setup[7]. Besides, the volatility of measured OOMs represented by the dots color showed negative relationship with the OSc, suggesting that the OOMs with high OSc might contributed more to SOA formation via condensation.

3.1.2 Temporal and diurnal variations

The time series of measured OOMs and related parameters are shown in Figure S1. During the campaign, the OOMs concentration ranged from 3.12×10^{7} to 7.90×10^{8} molecules cm^{-3} with a campaign average of 2.53×10^{8} molecules cm^{-3}, which was much higher than the levels observed in several urban sites in Beijing (8.3×10^{7} molecules cm^{-3}, Oct.-Nov. 2019), Shanghai (7.80×10^{7} molecules cm^{-3}, Nov. 2018), Nanjing (7.70×10^{7} molecules cm^{-3}, Nov. 2018) during the similar season[14, 59], but comparable to the levels observed in Beijing in summer (1.6×10^{8} molecules cm^{-3})[36]. The latitude of Hong Kong is lower than these regions, which endows Hong Kong a stronger solar radiation and higher temperature condition to promote the OOMs formation (Table S1). During the monitoring period, air masses influenced this regional background site were mainly from continental flows from south and east China (**Figure 2**a), dominated by air masses originated from East China sea (52%) and Eastern China (36%), with a small fraction of air flow from the

South China sea (12%) only in the autumn. The photochemical age of the air masses was estimated by $-Log_{10}(NO_x/NO_y)$[60], and was much higher for ECS (21.2 h) and EC (21.1 h) air masses than the SCS (2.5 h, Figure S2a). The transport of aged urban plumes and continental flows would affect the precursors and atmospheric oxidation conditions at the regional background site, and thus the OOMs concentration and composition. As shown in **Figure 2**b, the measured OOMs concentration and proportion of nitrogen species in the oceanic air flows was the lowest (1.05×10^8 molecules/cm^3, 45.5%), with less fraction of high C and O content species (Figure S3, 4), while the continental air masses clusters carried abundant precursors (Figure S2c) and longer photochemical age (Figure S2a), leading to 1.9-2.9 times higher OOMs concentrations and more OOMs species with high C and O content. In addition, the proportions of CHON, CHON2 and CHON3 OOMs in EC and ECS clusters were comparable but 13%, 4% and 0.2% respectively higher than the marine air masses (Figure S2b).

The diurnal pattern of measured OOMs is shown in **Figure 2c**. The OOMs concentration peaked at around 12:00 LT, then decreased slowly in the afternoon, and kept at a considerable level at night. Due to the short lifetime of OOMs (less than 1 hour via only condensation loss[7]), their variation would be largely affected by the oxidant levels. The morning increase and noon peak of OOMs was correlated with the simulated OH radicals, suggesting the important role of photochemical oxidation and OH-initiated oxidation process in OOMs formation. However, the slow decreasing trend of OOMs in the afternoon, along with the considerable levels in the evening, indicate the potential vital roles of ozone and NO_3 oxidations in OOMs formation, which is also supported by the better correlation of nocturnal OOMs and NO_3 radicals (Figure S5). The observed diurnal pattern of OOMs in Hong Kong was similar to the previous studies in several urban sites (like Beijing, Shanghai, and Nanjing in China)[14, 36, 61, 62], but different from that observed in some

boreal forest sites (i.e., Hyytiälä forest in Finland and Landes forest in French), where OOMs peaked in nighttime and were dominated by the monoterpene derived-OOMs[56, 63].

3.2 Influence of environmental factors on OOMs formation

As discussed above, environmental factors including temperature, solar radiation and NOx levels can affect the OOMs formation and composition. The solar radiation and temperature are usually coupled primary factors influence the degree of photochemical reactivity. **Figure 3**a compares the OSc distribution of OOMs concentration measured in the two phases. The fraction of high OSc OOMs species were higher in the first phase in accordance with higher temperature and solar radiation (26 °C and 150 W/m^2), whereas more OOMs distributed in lower OSc bins in second phase (21 °C and 91 W/m^2). Though the higher temperature would promote elevated biogenic emissions and result in change of precursors profiles and OOMs composition, the trends observed here could be possibly attributed to the accelerated RO_2 autoxidation process with the increase of temperature, which promotes the OOMs production with higher OSc. It was reported that a 20 K increment of temperature could increase 5-fold high of autoxidation reactions rates of RO_2[41]. Previous chamber studies observed higher total signals and more highly oxidized OOMs at higher temperature conditions [34, 35, 62]. As also shown in Figure S6, with the increase of solar radiation, the fraction of higher OSc species increased, proving that active photochemistry promotes the OOM formation and influence the composition and distribution. A recent study compared the ambient OOMs measurement at different location and seasons also suggested a consistent increase trends of OOMs concentration with temperature and global radiation[36]. Therefore, the formation of more highly oxidized OOMs is favored with higher temperature and solar radiation under similar precursor conditions.

253 The OSc distribution of OOMs under different NOx conditions is shown in **Figure 3**b. The OSc
254 fractions presented a Gaussian distribution pattern and peaked between -0.5 and 0.1. With the
255 increase of NOx, the OSc distribution of OOMs shifted from the high value to low value. As an
256 important terminator for RO_2 reactions, NO_x can affect the branching ratio between the
257 unimolecular autoxidation and bimolecular termination reactions, and terminate the RO_2 radical
258 in the early stage of autoxidation, thereby hindering the further oxidation and formation of higher
259 OSc OOMs[38, 41]. Though NOx suppressed the high OSc species formation, the concentration of
260 OOMs elevated with the increase of NOx (Figure S7). In polluted conditions, the high NOx was
261 always accompanied by high levels of anthropogenic VOCs as the key OOMs precursors, which
262 would result in more OOMs formation.

263 **Figure 3**c,d exhibits examples of the above-mentioned impacts on specific OOMs formation.
264 $C_7H_{11}NO_x$ (x=6, 8, 10, 12, 14) were reported as a series of α-pinene or aromatics oxidation
265 products with increased autoxidation steps[64]. The ratio of higher oxidation degree products,
266 $C_7H_{11}NO_x$ (x=8, 10, 12, 14), to $C_7H_{11}NO_6$ was used here to evaluate their relative increasement
267 and the influence of temperature and NOx on the autoxidation process. The ratios show an obvious
268 increase trend towards higher temperature and lower NOx, and similar patterns were also observed
269 for other groups of OOMs. The results demonstrate the acceleration of autoxidation and higher
270 OSc products formation under elevated temperature condition but the suppression effects under
271 high NOx conditions, though both temperature and NOx showed positive relations with overall
272 OOMs concentrations.

273 **3.3 PMF analysis on characterizing the complex OOMs species**

274 In view of the complex OOMs composition and formation pathways, PMF analysis was performed

to separate the measured OOMs species into different factors and to infer the plausible sources and formation pathways. A 6-factor solution was selected as a proper solution based on diagnostics of the solutions, evolution of multiple PMF solutions, interpretability and current knowledge of atmospheric oxidation processes. The detailed information on PMF diagnostics is provided in the SI. The mass spectra profiles of the resolved factors are shown in **Figure 4**, and detailed discussion of each profile is presented below.

Factor 1: The fingerprint peaks of this factor are species with four oxygen or two nitrogen atoms, including $C_7H_{10}O_4$, $C_5H_6O_4$, $C_8H_{12}O_4$ and $C_6H_{10}O_8N_2$, which are characterized with double bond equivalent (DBE) ≥ 3. The DBE of typical alkene and alkane are generally ≤ 2, and it is hard for them to form products with DBE of 3. Thus, aromatics are the most likely precursors for these species. In the traditional OH-initiated oxidation mechanism of aromatics (Figure S8), the OH radical would firstly add to benzene ring to generate phenol or bicyclic peroxy radical (BCP-peroxy). Subsequently, the BCP-peroxy could be either terminated directly by NO, NO_2, RO_2 radicals and HO_2, or produce bicyclic alkoxy radical (BCP-oxy) via reacting with NO. BCP-oxy could further react with O_2 to produce the ring-retaining O4 carbonyls products (containing C=O group; e.g., $C_6H_6O_4$ in Figure S8) with DBE of four, and this carbonyl products could also be formed from another RO_2 radical terminated reactions. The above mechanism could explain the formation of those O4 carbonyls with six or more carbon atoms. However, some C_5 species were observed in the benzene-OH oxidation system in recent chamber experiments and could not be deduced [28, 30]. Xu et al.[29] proposed a new ring-breakage pathway, in which 14% BCP-oxy could undergo CO-loss and O_2 addition in the ring opening process and result in the formation of a more saturated C_5 radicals in benzene oxidation process. Following this pathway, the newly generated RO_2 radical (with 1 less C atom) could continue to react with NO and O_2, or another RO_2 radical,

298 forming the ring-opening O4 carbonyls products with DBE of three (e.g., $C_5H_6O_4$ in Figure S8),
299 namely the fingerprint peaks in this factor. This factor presented relative constant levels in both
300 daytime and nighttime, and only a small trough at noon. The diurnal variability of this group seems
301 influenced by complex parameters and are not well understood currently, requiring further research.

302 **Daytime factor 2:** The second factor was a daytime factor with peaks around 15:00 LT. This factor
303 was dominated by some five oxygen OOMs in the series of $C_nH_{2n-4}O_5$ (n=6-9) and $C_nH_{2n-2}O_5$ (n=5-
304 8). Based on the above discussion on aromatics oxidation mechanism (Figure S8), the $C_nH_{2n-4}O_5$
305 series with the DBE of 3 are most likely the ring-retaining hydroperoxides (containing -COOH
306 group; e.g., $C_6H_8O_5$ in Figure S8) from the termination reaction of BCP-peroxy with HO_2.
307 Compared with $C_nH_{2n-4}O_5$ (n=6-9) series, the $C_nH_{2n-2}O_5$ (n=5-8) series have one-degree lower DBE
308 and one less nC, which could be the ring-opening hyperoxides from the CO-loss pathway and
309 terminated by HO_2 (e.g., $C_5H_8O_5$ in Figure S8).

310 **Daytime factor 3:** This factor was a daytime factor with double peaks appearing at around 12:00
311 LT and 18:00 LT, respectively. The high level of OH radicals in the noontime should be responsible
312 for the noon peak, while the urban plumes in the evening rush hour and NO_3 radicals should be
313 responsible for the dusk peaks. The profile was mostly featured by species with six oxygen and
314 one nitrogen, such as the series of $C_nH_{2n-5}NO_6$ (n=7-10), $C_nH_{2n-3}NO_6$ (n=5-10) and $C_nH_{2n-1}NO_6$
315 (n=4-9), with DBE of three, two and one, respectively. Following the discussion above and
316 oxidation mechanism in Figure S8, the fingerprint species with 1N in this factor are likely
317 contributed by NO termination pathway of RO_2 from different precursors. For example, $C_nH_{2n-5}NO_6$
318 (n=7-10), with three unsaturation degrees, were possibly the ring-retaining nitrates
319 (containing -ONO_2 group; e.g., $C_6H_7NO_6$ in Figure S8) generated from the termination reaction of
320 BCP-peroxy with NO. The $C_nH_{2n-3}NO_6$ (n=5-10) series, with one level lower in DBE, could be the

ring-opening nitrates from the CO-loss pathway in aromatics oxidation and then terminated by NO (e.g., $C_5H_7NO_6$). The oxidation of alkene and alkane were likely responsible for the formation of more saturated $C_nH_{2n-1}NO_6$ (n=4-9) species. In the ambient environment, RO_2 radical generated from the oxidation of alkenes (such as isoprene) and alkanes could also produce these fingerprint peaks (e.g., $C_5H_9NO_6$ and $C_6H_{11}NO_6$ in Figure S9 and S10).

Daytime factor 4: This factor shows a clear daytime peak at noon and is mainly characterized by species with seven oxygen and one nitrogen, including the series of $C_nH_{2n-5}NO_7$ (n=6-9) and $C_nH_{2n-3}NO_7$ (n=5-8) with DBE of three and two, respectively. Compared to the fingerprint species of $C_nH_{2n-5}NO_6$ in daytime factor 3, the series of $C_nH_{2n-5}NO_7$ (n=6-9) in this factor have same DBE but one more O atom, and are likely the ring-retaining peroxyl nitrates (containing -$OONO_2$ group) from the termination reaction of BCP-peroxy with NO_2 (e.g., $C_6H_7NO_7$ in Figure S8). Similarly, the intermediate RO_2 radicals of $C_nH_{2n-3}NO_7$ (n=5-8) were possibly generated from BCP-peroxy ring-breakage with CO-loss pathway, followed by termination reaction with NO_2 to form the peroxyl nitrates with one C less (e.g., $C_5H_7NO_7$ in Figure S8). In addition, $C_5H_9NO_7$ with DBE of one also showed a high fraction in this factor and is likely the peroxyl nitrate formed from the isoprene and alkane oxidation (Figure S9).

Daytime factor 5: This factor was identified as the di-nitrates factor with one afternoon peak at 15:00 LT and another evening peak presented around 18:00-22:00 LT. The fingerprint molecules of this factor contain two nitrogen atoms, including the series of $C_nH_{2n-2}N_2O_8$ (n=6-10) and $C_nH_{2n}N_2O_8$ (n=6-9) with DBE of one and zero, respectively. The afternoon peak could be mainly attributed to the multi-generation OH oxidation products, in which di-nitrates are second-generation products form further oxidation of first-generation nitrates and peroxyl nitrates. It is consistent with the delay of afternoon peak appearance of di-nitrates factor compared to factors

dominated by peroxyl nitrates and nitrates (daytime factor 3 and 4). The dusk peak was mainly contributed by the NO_3 oxidation, either the products from NO_3-initiated first generation RO_2 terminated by NOx, or second-generation NO_3 oxidation of first-generation nitrate and peroxyl nitrate products.

Nighttime factor 6: The biogenic factor showed a broad nighttime peak with an increasing trend after sunset and a decreasing trend after sunrise (6:00 LT), indicating the important role of nocturnal chemistry in their formation. A series of $C_{10}H_{13\text{-}19}N_{0\text{-}2}O_{5\text{-}8}$ accounted for high fraction in this profile and they were the typical oxidation products of the terpenes observed in chamber and field experiments[19, 65]. The terpenes could be oxidized by NO_3 radicals and O_3[66] and then contributed to the C_{10} N-containing OOMs formation (Figure S11). Similar nighttime factors dominated by C_{10} terpenes oxidation has been observed at a boreal forest site[44]. Most fingerprint molecules observed in this factor are nitrous OOMs, and are consistent with the nighttime BVOC factors identified in suburban Nanjing with higher fraction of organic nitrates[12]. It is worth noting that these $C_{10}H_{13\text{-}19}N_{0\text{-}2}O_{5\text{-}8}$ molecules also presented in the daytime factors (e.g., daytime factor 3), and part of them could be formed from daytime OH-initiated reactions.

3.4. A simplified categorization scheme for OOMs

Though the PMF analysis is powerful in extracting information from complex ambient data with prior unknown chemistry and processes, the diagnostics of the solutions and factor interpretation can be very effort- and time-consuming. Thus, inspired from the characteristics of above PMF factors, a simple classification method was developed to identify the key functional groups and termination reaction pathways of measured OOMs in this study. The new method categorizes the OOMs according to the revealed characteristics of fingerprint peaks in each factor, as summarized in Table S2. Though the concentration of those multi-generation oxidation products with more O

atoms were very low and not clearly discussed in the PMF analysis, they are also accounted and can be classified in the scheme. In brief, the non-nitrogen species with DBE of 2 and 3 and O atoms of 2n+4 (n=0,1,..) are classified as carbonyls, and the non-nitrogen species with DBE of 1-3 and O atoms of 2n+5 (n=0,1,..) are classified as hydroperoxides. For the 1N OOMs with DBE of 1-3, the species with O atoms of 2n+6 (n=0,1,..) and 2n+7 (n=0,1,..) are classified as nitrates and peroxyl nitrates, respectively. The species with DBE ≥ 4 were recognized as aromatic ring-retaining species, which was not resolved in PMF results but they could be easily identified and distinguished from others. The OOMs with 10 C atoms was categorized as terpene-derived OOMs. Although we could not exclude the possibility of some C10 species from aromatics or aliphatic precursors, the majority OOMs (>80%) in this group should be related to terpene considering its relatively higher concentration (154 ppt), higher oxidation rates than other precursors at this background site, and good consistency with the peak list from previous chamber and field studies (Table S3). It should be noted that this approach is more suitable for application in similar environmental conditions as the present study, and uncertainties may still exist in this simplified approach because the complexity of the processes and chemical reactions in the real atmosphere.

As shown in **Figure 5**a, a total 66% of measured OOMs species can be categorized into these seven groups: carbonyls (7%), hydroperoxides (7%), nitrates (17%), peroxyl nitrates (10%), terpenes (7%), di-nitrates (12%) and aromatic ring-retaining species (6%). The nitrates accounted for the highest proportion, which echoes another measurement in suburban Nanjing that reported organic nitrates as the dominant OOMs in the daytime[12]. Terpenes-derived OOMs were the dominant species in boreal forest sites in Europe [67-69], and only contributed 7% to the OOMs formation in Hong Kong, reflecting the significant differences in OOMs composition between urban and remote areas.

3.5 OOMs volatility estimation based on the classified results

Due to the lake of molecular information on functional groups, the volatility of OOMs were usually estimated by parameterization method in previous studies with assumptions in the fixed types and distribution of functional groups[13, 14, 52]. In the above analysis, the functional groups in the observed OOMs are largely affected by oxidation pathways and might be different from the assumptions (Table S4), leading to uncertainties in OOMs volatilities estimation in the real atmosphere. Based on the OOMs categorization in the present study, the functional groups in the OOM molecules were roughly identified (detailed information is shown in SI), and OOMs volatility can then be estimated with the SIMPOL.1 method[53] (**Figure 5**b). The results show that most of carbonyls, hydroperoxides, nitrates, peroxyl nitrates and aromatic ring-retaining species are SVOC and intermediate VOC (IVOC) with total proportion of 82%, 75%, 82%, 86% and 58%, respectively. In contrast, most of di-nitrates and terpenes-derived OOMs are extremely low-volatility organic compounds (ELVOC) and low-volatility organic compounds (LVOC) with the proportion of 78% and 70%, respectively.

The ELVOC, LVOC, SVOC and IVOC accounted for 8%, 20%, 51% and 20% of the measured OOMs, respectively. Compared with results estimated from parameterization method of Donohue et al.[52], the ELVOC decreases by 5% but IVOC increases by 5%, while the LVOC and SVOC are similar, suggesting the possible overestimation in ELVOC and underestimation in IVOC by the parameterization method (Figure S12a). The volatility of each category OOMs calculated by two methods are compared in Figure S12b. For the improved volatility estimation with functional groups information, the mean volatility of all OOMs increase by 0.67 order of magnitude, with 2.3, 4.4, 1.1, 3.2, and 1.4 order of magnitude increase for carbonyls, hydroperoxides, nitrates, peroxyl nitrates and terpenes respectively, but 0.7 and 2.8 order of magnitude decrease for aromatic

ring-retaining species and di-nitrates. The discrepancy is mainly due to the roughly assumption of constant relative fraction of limited oxygenated functional groups (such as -OH and C=O groups) and underestimation of -OOH and different nitrate groups. More studies have recognized the important role of -OOH groups formed from autooxidation step in OOMs[8], which is also demonstrated in the present study. The more counts of -OH group rather than -OOH group in OOMs would result in underestimation of volatility in parameterization methods, and the neglect of the nitrate groups in di-nitrates, $-NO_2$ group on aromatic ring-retaining species and aromatic rings would lead to overestimation of their volatilities. Though uncertainties still exist in the multifunctional groups identification in this simple classification approach, our attempts provide some new insights and feasible routes to improve the volatility estimation of complex OOMs in real atmosphere.

3.6 Contribution of OOMs to particles growth

The low volatile nature of the OOMs make it vulnerable to partition and condense onto particle phase, thus contributing to particle growth and SOA formation. During the campaign, we observed several cases (e.g., 29th November, 17th December and 19th December 2018) with relative high concentrations of OOMs accompanied with clear particle growth process, mainly under the influences of continental transport flows. The growth of newly formed particles started at the same time when OOMs peaked at noon, implying that OOMs may play a significant role in the particle growth process. Based on the improved volatility estimation, the irreversible condensation of OOMs and gas-particle equilibrium partitioning were calculated to evaluate the OOMs contribution to particles growth rate (GR).

As shown in the new particle formation and growth case from 13:00 on 17th December to 10:00

on 18th December 2018 (**Figure 6**a), the particle mobility diameter grew from 20 to 70 nm in around 20 hours. Given the initial mobility diameter, the temporal evolution of particle size growth was estimated from the aerosol growth model, and the simulated results exhibit good agreement with the observed particle growth pattern, demonstrating the dominated role of OOMs in this particle growth case from 20 to 70 nm. The size-dependent condensation contribution of different OOMs groups and sulfuric acid on the particle GR is shown in **Figure 6**b. With the increase of particle diameter from 15 to 700 nm, GR of particles decreased from 2.7 nm/h to 0.9 nm/h. In contrast to the more predominant role of sulfuric acid on particle growth of newly formed particles (< 3 nm)[13], the condensable organic species contribute more exceeding role in the particle growth of larger particles. This is also consistent with our previously reported dominant contribution of OOMs to SOA formation, in which the irreversible condensation of observed OOMs can explain 68% of SOA growth rate.[14]

Di-nitrates and aromatic ring-retaining species were the two most important contributors to GR with a fraction of 44.0% and 10.4%, though their concentration only accounted for 14.0% and 6.3% of the measured OOMs during the case period. The contribution of carbonyls, hydroperoxides, nitrates, peroxyl nitrates, terpenes and sulfuric acid to GR were 3.5%, 4.0%, 2.7%, 1.2%, 4.4% and 0.1%, respectively. The unclassified OOMs also have a large (30%) contribution to the growth rate. Though the functional groups cannot be identified in this group, but the key feature of those molecules still indicates their anthropogenic nature, mostly from aromatic and aliphatic precursors. Meanwhile, the contribution of SVOCs via equilibrium partitioning was negligible in contributing the particle growth. Another two NPF and growth cases were also examined (Figure S13) and showed similar results. Moreover, for comparison we also simulated the particle growth in the case using the volatility derived from parameterization method (Figure S14), and the simulated results

apparently overestimate the GR compared to the observed particle growth. The results demonstrate the value of the developed classification scheme for OOMs characterizations. Further efforts are still warranted to better elucidate the OOMs and formation pathways at the molecular level under different precursors, oxidants, and environmental conditions. The quantitative information of the multifunctional groups is crucial for better evaluating the contributions of OOMs on particle growth and SOA formation, demonstrating the value of the developed classification scheme for OOMs characterizations.

Overall, this study provides a comprehensive molecular analysis of the composition, variation characteristics, and formation pathways of oxygenated organic molecules (OOMs) formed from a cocktail of anthropogenic precursors in an urbanized region. The findings offer new molecular-level insights shed light into the formation and fate of OOMs in the polluted atmosphere, and improve our understanding of the complex VOC oxidation and secondary pollution formation in polluted urban regions, which has important implications for the development of air pollution mitigation strategies.

Figures

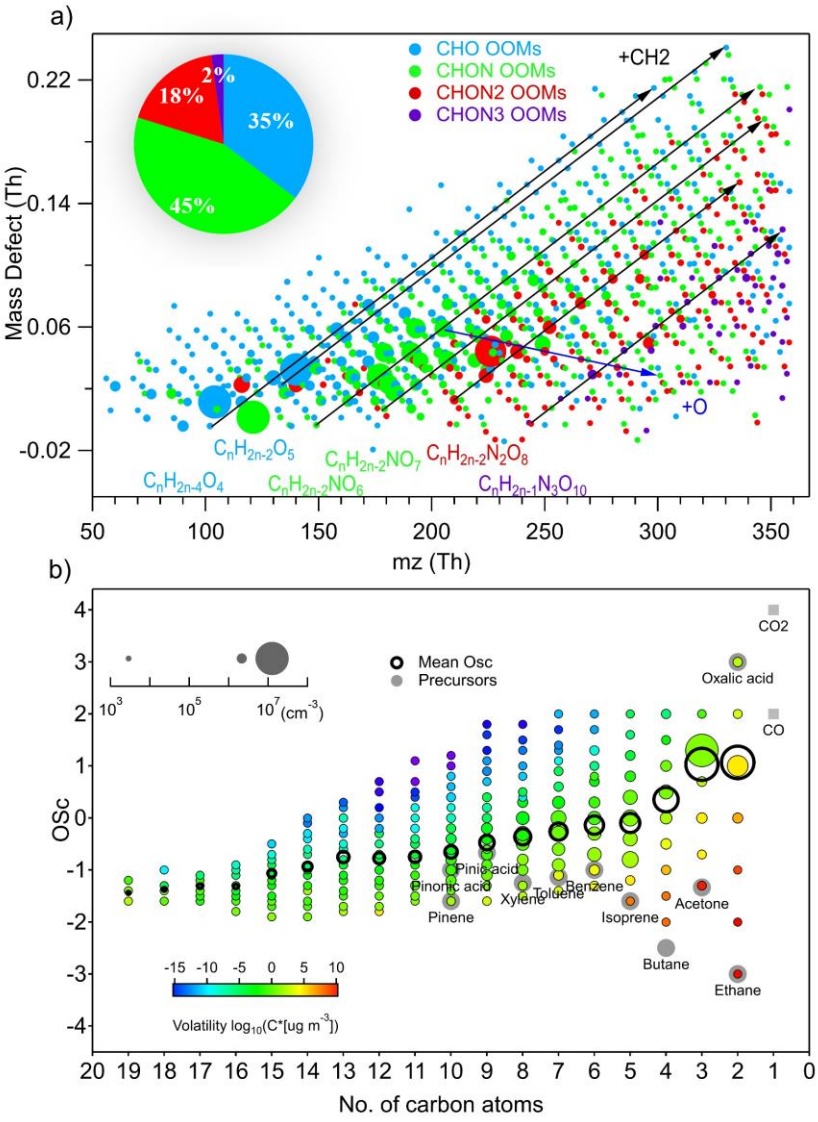

Figure 1. a) Mass defect plot of the oxygenated organic molecules (OOMs) identified from the NO3-CI-ToF-MS measurements in the field campaign in Hong Kong. The dots are colored with the nitrogen numbers and scaled by the concentration. The dots connected by arrow lines represent the homologs. b) The OSc distribution of OOMs as a function of carbon number (nC). The dots are colored with the OOMs volatility and scaled by the concentration. The black circle denotes the concentration-weighted mean OSc of measured OOMs for each carbon number. Some OOMs precursors labelled by gray symbols are also shown for reference.

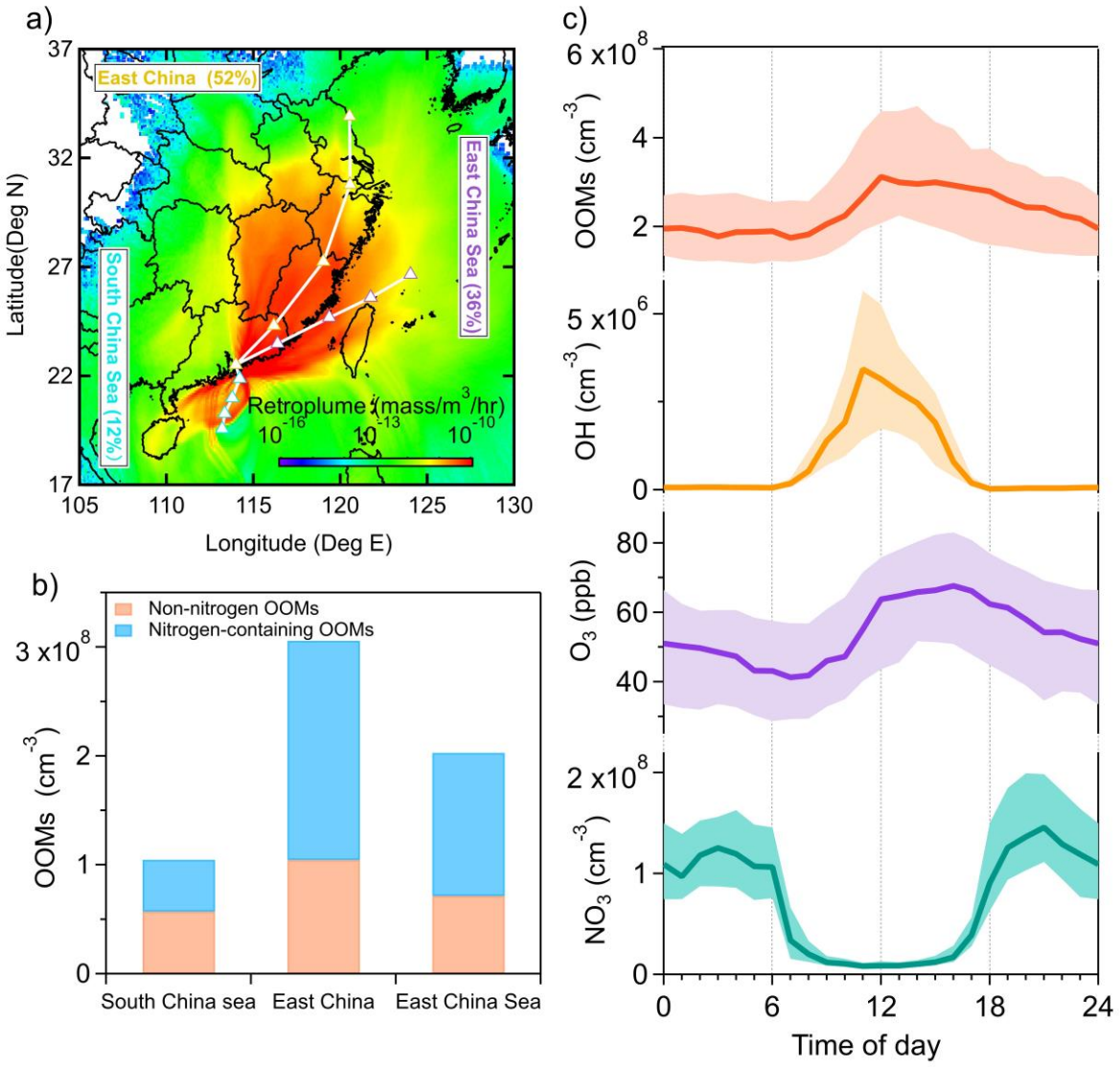

Figure 2. (a) The map of 72h backward footprint (100m) retroplume and trajectories arriving at the monitoring site simulated with the Hybrid Single-particle Lagrangian Integrated Trajectory (HYSPLIT). (b) Comparison of measured OOMs concentration and non-nitrogen and nitrogen-containing fractions under different air mass trajectory clusters. Detailed setting of HYSPLIT footprint retroplume can be found in the SI. (c) Diurnal patterns of the measured OOMs, ozone, and estimated OH and NO_3 radicals during the campaign in Hong Kong. The OH radical and NO_3 are simulated with an observation-based photochemical box model based on MCM 3.3. The lines represent the median values, and the areas denote the 75th and 25th percentile of the data, respectively.

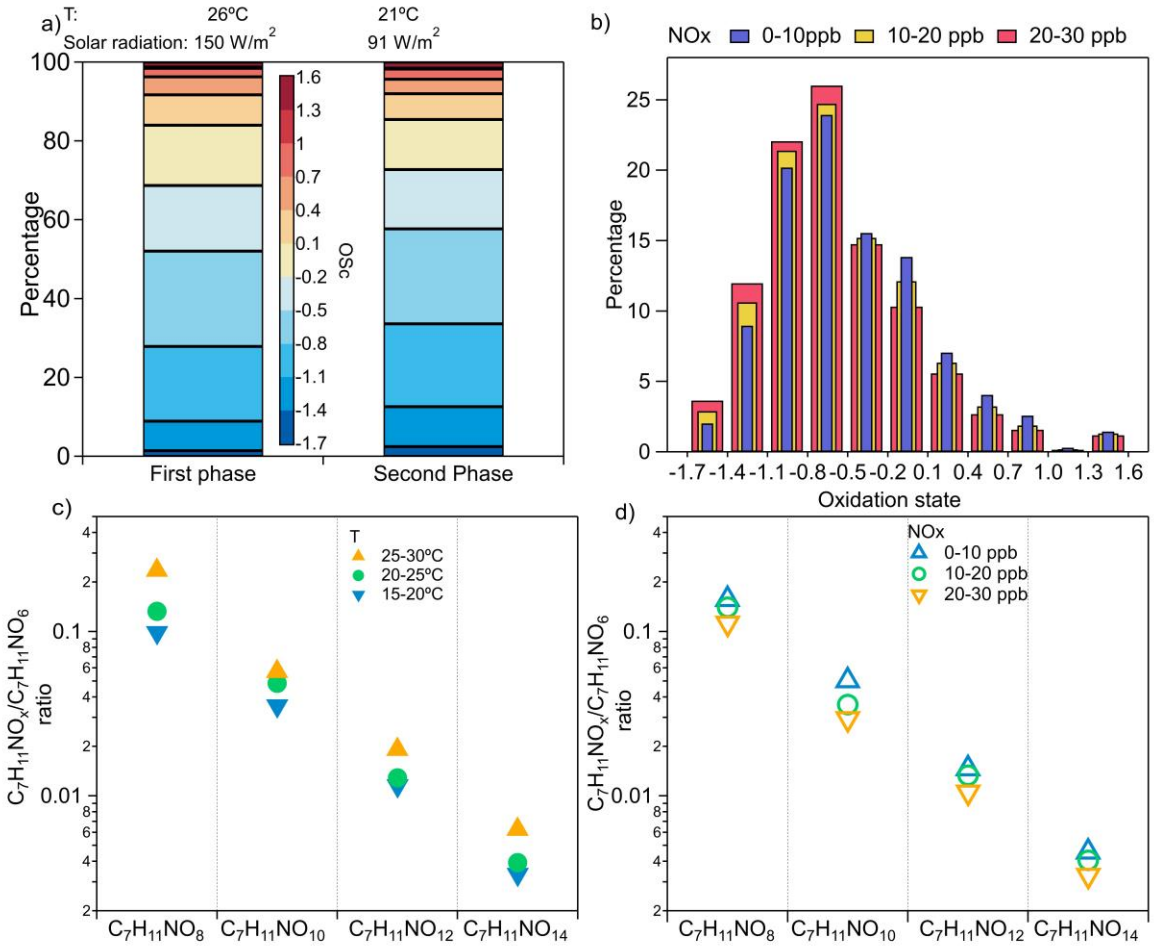

Figure 3. The impact of temperature and NOx on OOMs OSc and formation. a) The OOMs OSc distribution in Autumn and winter, the bar was colored with OOMs OSc degree. b) The OOMs OSc distribution in different NOx conditions. c,d) A specific example, $C_7H_{11}NO_{6,8,10,12,14}$ series, to show the influence of temperature and NOx on products with different autoxidation steps.

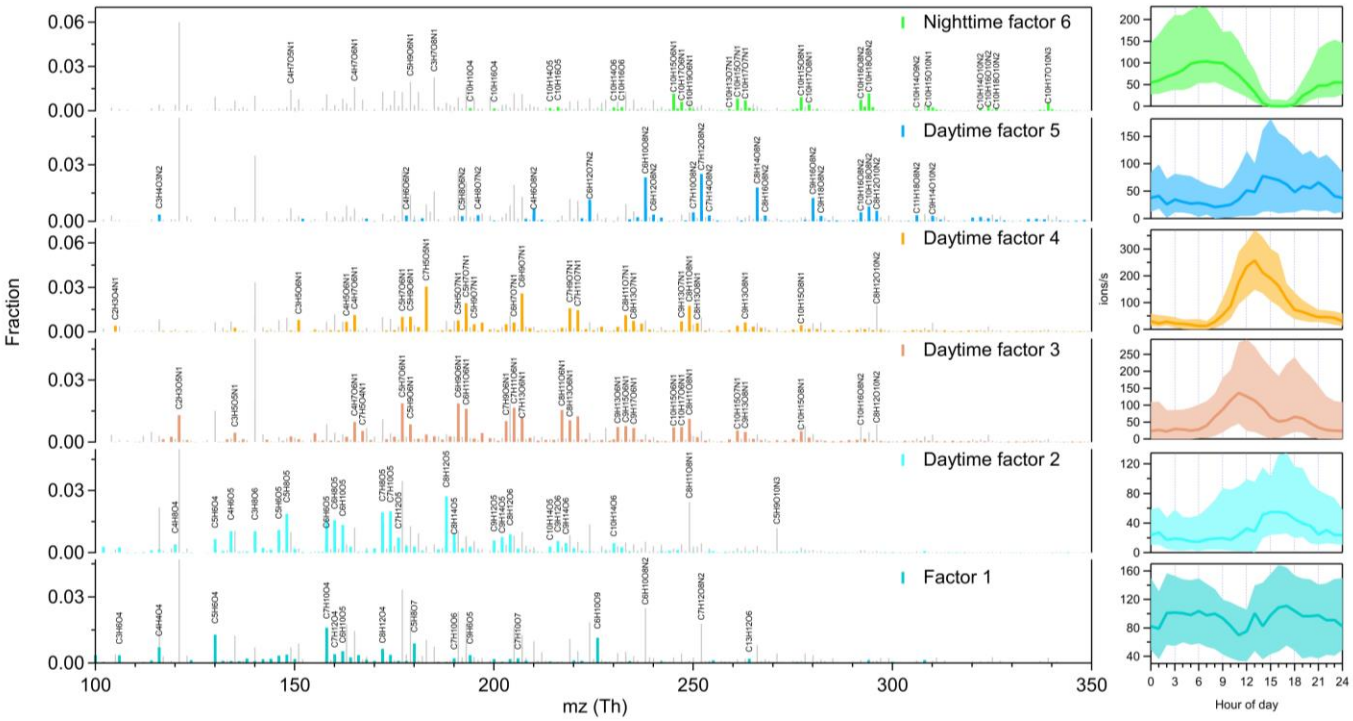

Figure 4. The profiles and diurnal patterns of PMF factor. The fingerprint peaks of each factor are highlighted, and their formulas are also marked. The three lines in the diurnal plot represent median values, 25th and 75th percentiles,

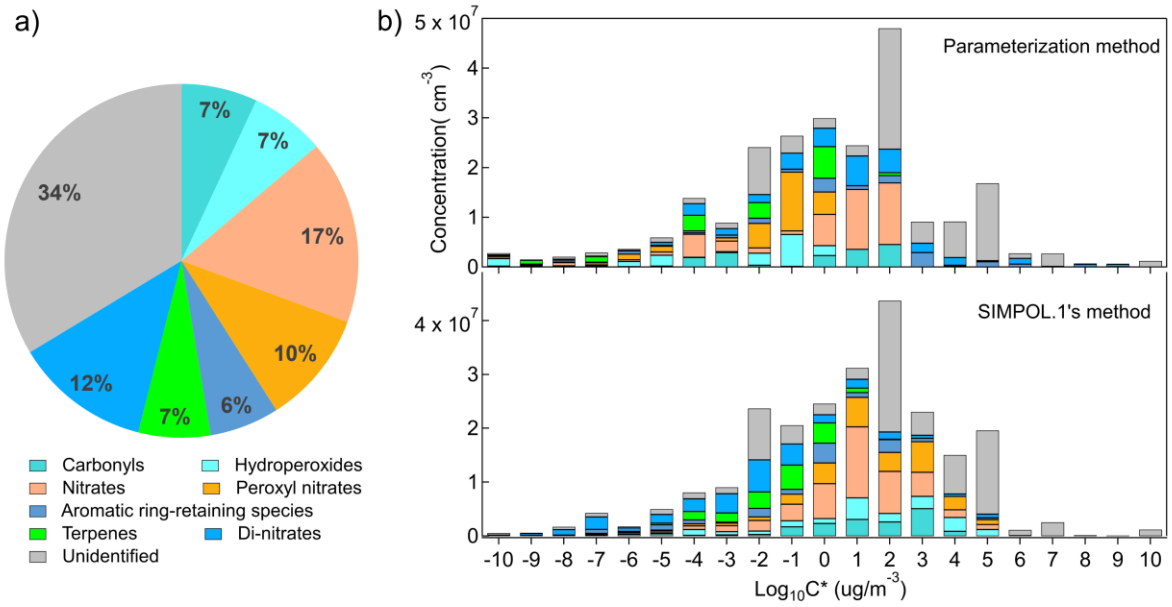

503

504 **Figure 5.** (a) The proportion of OOMs species that categorized by the new metrics in Table S2. (b)
505 The comparison of volatility distribution calculated with new method and parameterization method.

506

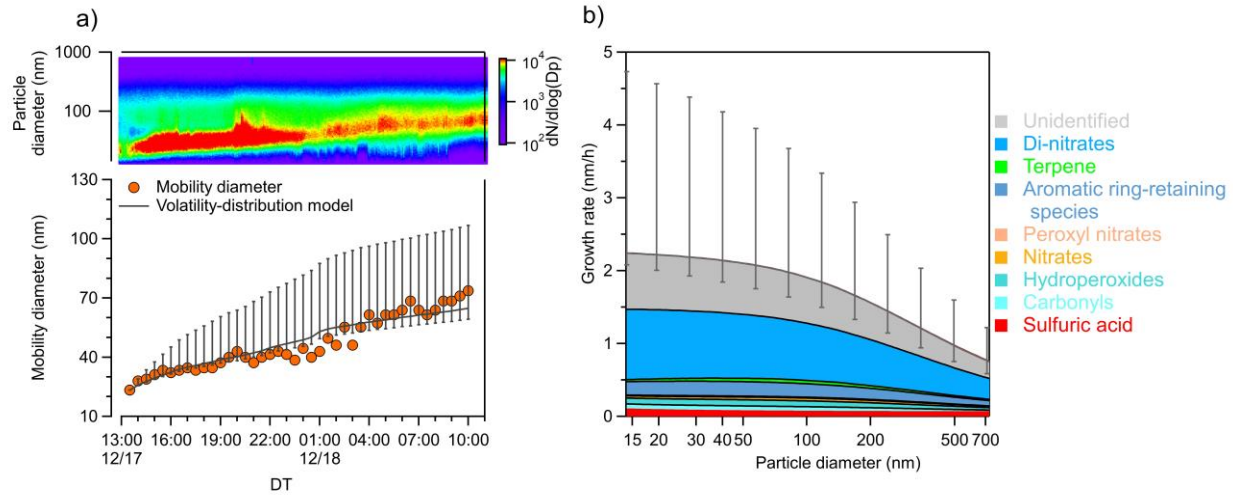

507

508 **Figure 6.** A particle formation and growth case observed during the campaign to evaluate the
509 OOMs contributions to the particle growth rate. (a) The upper panel shows the measured particle
510 distribution in a NPF case during 17^{th}-18^{th} December 2018, and the lower panel displays the
511 temporal evolution of measured particle mobility diameter (red dots) and simulated particle size
512 (line). Error bar represents the maximum uncertainty introduced by the assumption of the extreme
513 parameter Xi,p (the mass fraction of OOMs species in the particle phase) in the aerosol growth
514 model. (b) The contribution of classified OOMs groups on particle growth rate as a function of
515 particle size.

Associated Content

Supporting Information.

The following files are available on the ACS Publications website. NO_3-ToF-CIMS instrument settings, calibration and transmission; PMF model settings and solution diagnostics; OOMs volatility and OSc estimation methods; Deduction of OOMs functional groups; Aerosol growth model introduction; supplemental figures and tables (PDF).

Author Information

Corresponding Author

*Zhe Wang: z.wang@ust.hk

Notes

The authors declare no competing financial interest.

Acknowledgment

This study is supported by the Research Grants Council (RGC) of Hong Kong Special Administrative Region, China (T24-504/17-N, 16209022), National Natural Science Foundation of China (42122062), Hong Kong Environment and Conservation Fund (project 125/2020), and HKUST IPO support fund for interdisciplinary research collaboration. The authors would like to acknowledge the HKPolyU University Research Facility in Chemical and Environmental Analysis (UCEA) for the equipment support, and Hong Kong Environmental Protection Department for providing access to the Cape D'Aguilar Supersite AQMS and for sharing the trace gases, particles and VOCs data at the Supersite.

References

1. IPCC, Climate Change 2007 Synthesis Report. **2007**.

2. Park, M.; Joo, H. S.; Lee, K.; Jang, M.; Kim, S. D.; Kim, I.; Borlaza, L. J. S.; Lim, H.; Shin, H.; Chung, K. H.; Choi, Y. H.; Park, S. G.; Bae, M. S.; Lee, J.; Song, H.; Park, K., Differential toxicities of fine particulate matters from various sources. *Scientific reports* **2018,** *8*, (1), 17007.

3. Carlton, A. G.; Wiedinmyer, C.; Kroll, J. H., A review of Secondary Organic Aerosol (SOA) formation from isoprene. *Atmospheric Chemistry and Physics* **2009,** *9*, (14), 4987-5005.

4. Ziemann, P. J.; Atkinson, R., Kinetics, products, and mechanisms of secondary organic aerosol formation. *Chem Soc Rev* **2012,** *41*, (19), 6582-605.

5. Ghirardo, A.; Xie, J. F.; Zheng, X. H.; Wang, Y. S.; Grote, R.; Block, K.; Wildt, J.; Mentel, T.; Kiendler-Scharr, A.; Hallquist, M.; Butterbach-Bahl, K.; Schnitzler, J. P., Urban stress-induced biogenic VOC emissions and SOA-forming potentials in Beijing. *Atmospheric Chemistry and Physics* **2016,** *16*, (5), 2901-2920.

6. Noziere, B.; Kalberer, M.; Claeys, M.; Allan, J.; D'Anna, B.; Decesari, S.; Finessi, E.; Glasius, M.; Grgic, I.; Hamilton, J. F.; Hoffmann, T.; Iinuma, Y.; Jaoui, M.; Kahnt, A.; Kampf, C. J.; Kourtchev, I.; Maenhaut, W.; Marsden, N.; Saarikoski, S.; Schnelle-Kreis, J.; Surratt, J. D.; Szidat, S.; Szmigielski, R.; Wisthaler, A., The molecular identification of organic compounds in the atmosphere: state of the art and challenges. *Chemical reviews* **2015,** *115*, (10), 3919-83.

7. Bianchi, F.; Kurten, T.; Riva, M.; Mohr, C.; Rissanen, M. P.; Roldin, P.; Berndt, T.; Crounse, J. D.; Wennberg, P. O.; Mentel, T. F.; Wildt, J.; Junninen, H.; Jokinen, T.; Kulmala, M.; Worsnop, D. R.; Thornton, J. A.; Donahue, N.; Kjaergaard, H. G.; Ehn, M., Highly Oxygenated Organic Molecules (HOM) from Gas-Phase Autoxidation Involving Peroxy Radicals: A Key Contributor to Atmospheric Aerosol. *Chemical reviews* **2019,** *119*, (6), 3472-3509.

8. Ehn, M.; Thornton, J. A.; Kleist, E.; Sipila, M.; Junninen, H.; Pullinen, I.; Springer, M.; Rubach, F.; Tillmann, R.; Lee, B.; Lopez-Hilfiker, F.; Andres, S.; Acir, I. H.; Rissanen, M.; Jokinen, T.; Schobesberger, S.; Kangasluoma, J.; Kontkanen, J.; Nieminen, T.; Kurten, T.; Nielsen, L. B.; Jorgensen, S.; Kjaergaard, H. G.; Canagaratna, M.; Maso, M. D.; Berndt, T.; Petaja, T.; Wahner, A.; Kerminen, V. M.; Kulmala, M.; Worsnop, D. R.; Wildt, J.; Mentel, T. F., A large source of low-volatility secondary organic aerosol. *Nature* **2014,** *506*, (7489), 476-9.

9. Jokinen, T.; Berndt, T.; Makkonen, R.; Kerminen, V. M.; Junninen, H.; Paasonen, P.; Stratmann, F.; Herrmann, H.; Guenther, A. B.; Worsnop, D. R.; Kulmala, M.; Ehn, M.; Sipila, M., Production of extremely low volatile organic compounds from biogenic emissions: Measured yields and atmospheric implications. *Proceedings of the National Academy of Sciences of the United States of America* **2015,** *112*, (23), 7123-8.

10. Chrit, M.; Sartelet, K.; Sciare, J.; Pey, J.; Marchand, N.; Couvidat, F.; Sellegri, K.; Beekmann, M., Modelling organic aerosol concentrations and properties during ChArMEx summer campaigns of 2012 and 2013 in the western Mediterranean region. *Atmospheric Chemistry and Physics* **2017,** *17*, (20), 12509-12531.

11. Huang, X.; Zhou, L. X.; Ding, A. J.; Qi, X. M.; Nie, W.; Wang, M. H.; Chi, X. G.; Petaja, T.; Kerminen, V. M.; Roldin, P.; Rusanen, A.; Kulmala, M.; Boy, M., Comprehensive modelling study on observed new particle formation at the SORPES station in Nanjing, China. *Atmospheric*

Chemistry and Physics **2016,** *16*, (4), 2477-2492.

12. Liu, Y. L.; Nie, W.; Li, Y. Y.; Ge, D. F.; Liu, C.; Xu, Z. N.; Chen, L. D.; Wang, T. Y.; Wang, L.; Sun, P.; Qi, X. M.; Wang, J. P.; Xu, Z.; Yuan, J.; Yan, C.; Zhang, Y. J.; Huang, D. D.; Wang, Z.; Donahue, N. M.; Worsnop, D.; Chi, X. G.; Ehn, M.; Ding, A. J., Formation of condensable organic vapors from anthropogenic and biogenic volatile organic compounds (VOCs) is strongly perturbed by NOx in eastern China. *Atmospheric Chemistry and Physics* **2021,** *21*, (19), 14789-14814.

13. Qiao, X.; Yan, C.; Li, X.; Guo, Y.; Yin, R.; Deng, C.; Li, C.; Nie, W.; Wang, M.; Cai, R.; Huang, D.; Wang, Z.; Yao, L.; Worsnop, D. R.; Bianchi, F.; Liu, Y.; Donahue, N. M.; Kulmala, M.; Jiang, J., Contribution of Atmospheric Oxygenated Organic Compounds to Particle Growth in an Urban Environment. *Environmental science & technology* **2021,** *55*, (20), 13646-13656.

14. Nie, W.; Yan, C.; Huang, D. D.; Wang, Z.; Liu, Y.; Qiao, X.; Guo, Y.; Tian, L.; Zheng, P.; Xu, Z.; Li, Y.; Xu, Z.; Qi, X.; Sun, P.; Wang, J.; Zheng, F.; Li, X.; Yin, R.; Dallenbach, K. R.; Bianchi, F.; Petäjä, T.; Zhang, Y.; Wang, M.; Schervish, M.; Wang, S.; Qiao, L.; Wang, Q.; Zhou, M.; Wang, H.; Yu, C.; Yao, D.; Guo, H.; Ye, P.; Lee, S.; Li, Y. J.; Liu, Y.; Chi, X.; Kerminen, V.-M.; Ehn, M.; Donahue, N. M.; Wang, T.; Huang, C.; Kulmala, M.; Worsnop, D.; Jiang, J.; Ding, A., Secondary organic aerosol formed by condensing anthropogenic vapours over China's megacities. *Nature Geoscience* **2022,** *15*, (4), 255-261.

15. Wang, Y.; Clusius, P.; Yan, C.; Dallenbach, K.; Yin, R.; Wang, M.; He, X. C.; Chu, B.; Lu, Y.; Dada, L.; Kangasluoma, J.; Rantala, P.; Deng, C.; Lin, Z.; Wang, W.; Yao, L.; Fan, X.; Du, W.; Cai, J.; Heikkinen, L.; Tham, Y. J.; Zha, Q.; Ling, Z.; Junninen, H.; Petaja, T.; Ge, M.; Wang, Y.; He, H.; Worsnop, D. R.; Kerminen, V. M.; Bianchi, F.; Wang, L.; Jiang, J.; Liu, Y.; Boy, M.; Ehn, M.; Donahue, N. M.; Kulmala, M., Molecular Composition of Oxygenated Organic Molecules and Their Contributions to Organic Aerosol in Beijing. *Environmental science & technology* **2022,** *56*, (2), 770-778.

16. Almeida, J.; Schobesberger, S.; Kurten, A.; Ortega, I. K.; Kupiainen-Maatta, O.; Praplan, A. P.; Adamov, A.; Amorim, A.; Bianchi, F.; Breitenlechner, M.; David, A.; Dommen, J.; Donahue, N. M.; Downard, A.; Dunne, E.; Duplissy, J.; Ehrhart, S.; Flagan, R. C.; Franchin, A.; Guida, R.; Hakala, J.; Hansel, A.; Heinritzi, M.; Henschel, H.; Jokinen, T.; Junninen, H.; Kajos, M.; Kangasluoma, J.; Keskinen, H.; Kupc, A.; Kurten, T.; Kvashin, A. N.; Laaksonen, A.; Lehtipalo, K.; Leiminger, M.; Leppa, J.; Loukonen, V.; Makhmutov, V.; Mathot, S.; McGrath, M. J.; Nieminen, T.; Olenius, T.; Onnela, A.; Petaja, T.; Riccobono, F.; Riipinen, I.; Rissanen, M.; Rondo, L.; Ruuskanen, T.; Santos, F. D.; Sarnela, N.; Schallhart, S.; Schnitzhofer, R.; Seinfeld, J. H.; Simon, M.; Sipila, M.; Stozhkov, Y.; Stratmann, F.; Tome, A.; Trostl, J.; Tsagkogeorgas, G.; Vaattovaara, P.; Viisanen, Y.; Virtanen, A.; Vrtala, A.; Wagner, P. E.; Weingartner, E.; Wex, H.; Williamson, C.; Wimmer, D.; Ye, P.; Yli-Juuti, T.; Carslaw, K. S.; Kulmala, M.; Curtius, J.; Baltensperger, U.; Worsnop, D. R.; Vehkamaki, H.; Kirkby, J., Molecular understanding of sulphuric acid-amine particle nucleation in the atmosphere. *Nature* **2013,** *502*, (7471), 359-363.

17. Kirkby, J.; Curtius, J.; Almeida, J.; Dunne, E.; Duplissy, J.; Ehrhart, S.; Franchin, A.; Gagne, S.; Ickes, L.; Kurten, A.; Kupc, A.; Metzger, A.; Riccobono, F.; Rondo, L.; Schobesberger, S.; Tsagkogeorgas, G.; Wimmer, D.; Amorim, A.; Bianchi, F.; Breitenlechner, M.; David, A.; Dommen, J.; Downard, A.; Ehn, M.; Flagan, R. C.; Haider, S.; Hansel, A.; Hauser, D.; Jud, W.; Junninen, H.; Kreissl, F.; Kvashin, A.; Laaksonen, A.; Lehtipalo, K.; Lima, J.; Lovejoy, E. R.; Makhmutov, V.; Mathot, S.; Mikkila, J.; Minginette, P.; Mogo, S.; Nieminen, T.; Onnela, A.; Pereira, P.; Petaja, T.; Schnitzhofer, R.; Seinfeld, J. H.; Sipila, M.; Stozhkov, Y.; Stratmann, F.; Tome, A.; Vanhanen, J.;

Viisanen, Y.; Vrtala, A.; Wagner, P. E.; Walther, H.; Weingartner, E.; Wex, H.; Winkler, P. M.; Carslaw, K. S.; Worsnop, D. R.; Baltensperger, U.; Kulmala, M., Role of sulphuric acid, ammonia and galactic cosmic rays in atmospheric aerosol nucleation. *Nature* **2011,** *476*, (7361), 429-33.

18. Riccobono, F.; Schobesberger, S.; Scott, C. E.; Dommen, J.; Ortega, I. K.; Rondo, L.; Almeida, J.; Amorim, A.; Bianchi, F.; Breitenlechner, M.; David, A.; Downard, A.; Dunne, E. M.; Duplissy, J.; Ehrhart, S.; Flagan, R. C.; Franchin, A.; Hansel, A.; Junninen, H.; Kajos, M.; Keskinen, H.; Kupc, A.; Kurten, A.; Kvashin, A. N.; Laaksonen, A.; Lehtipalo, K.; Makhmutov, V.; Mathot, S.; Nieminen, T.; Onnela, A.; Petaja, T.; Praplan, A. P.; Santos, F. D.; Schallhart, S.; Seinfeld, J. H.; Sipila, M.; Spracklen, D. V.; Stozhkov, Y.; Stratmann, F.; Tome, A.; Tsagkogeorgas, G.; Vaattovaara, P.; Viisanen, Y.; Vrtala, A.; Wagner, P. E.; Weingartner, E.; Wex, H.; Wimmer, D.; Carslaw, K. S.; Curtius, J.; Donahue, N. M.; Kirkby, J.; Kulmala, M.; Worsnop, D. R.; Baltensperger, U., Oxidation products of biogenic emissions contribute to nucleation of atmospheric particles. *Science* **2014,** *344*, (6185), 717-21.

19. Nah, T.; Sanchez, J.; Boyd, C. M.; Ng, N. L., Photochemical Aging of alpha-pinene and beta-pinene Secondary Organic Aerosol formed from Nitrate Radical Oxidation. *Environmental science & technology* **2016,** *50*, (1), 222-31.

20. Berndt, T.; Richters, S.; Jokinen, T.; Hyttinen, N.; Kurten, T.; Otkjaer, R. V.; Kjaergaard, H. G.; Stratmann, F.; Herrmann, H.; Sipila, M.; Kulmala, M.; Ehn, M., Hydroxyl radical-induced formation of highly oxidized organic compounds. *Nature communications* **2016,** *7*, 13677.

21. Guo, Y. D.; Shen, H. R.; Pullinen, I.; Luo, H.; Kang, S.; Vereecken, L.; Fuchs, H.; Hallquist, M.; Acir, I. H.; Tillmann, R.; Rohrer, F.; Wildt, J.; Kiendler-Scharr, A.; Wahner, A.; Zhao, D. F.; Mentel, T. F., Identification of highly oxygenated organic molecules and their role in aerosol formation in the reaction of limonene with nitrate radical. *Atmospheric Chemistry and Physics* **2022,** *22*, (17), 11323-11346.

22. Wennberg, P. O.; Bates, K. H.; Crounse, J. D.; Dodson, L. G.; McVay, R. C.; Mertens, L. A.; Nguyen, T. B.; Praske, E.; Schwantes, R. H.; Smarte, M. D.; St Clair, J. M.; Teng, A. P.; Zhang, X.; Seinfeld, J. H., Gas-phase reactions of isoprene and its major oxidation products. *Chem. Rev.* **2018,** *118*, (7), 3337-3390.

23. Berndt, T.; Hyttinen, N.; Herrmann, H.; Hansel, A., First oxidation products from the reaction of hydroxyl radicals with isoprene for pristine environmental conditions. *Communications Chemistry* **2019,** *2*, (1), 10.

24. Ji, Y.; Zhao, J.; Terazono, H.; Misawa, K.; Levitt, N. P.; Li, Y.; Lin, Y.; Peng, J.; Wang, Y.; Duan, L.; Pan, B.; Zhang, F.; Feng, X.; An, T.; Marrero-Ortiz, W.; Secrest, J.; Zhang, A. L.; Shibuya, K.; Molina, M. J.; Zhang, R., Reassessing the atmospheric oxidation mechanism of toluene. *Proceedings of the National Academy of Sciences of the United States of America* **2017,** *114*, (31), 8169-8174.

25. Klotz, B. r.; Volkamer, R.; Hurley, M. D.; Andersen, M. P. S.; Nielsen, O. J.; Barnes, I.; Imamura, T.; Wirtz, K.; Becker, K.-H.; Platt, U.; Wallington, T. J.; Washida, N., OH-initiated oxidation of benzene. *Physical Chemistry Chemical Physics* **2002,** *4*, (18), 4399-4411.

26. Wang, L.; Wu, R.; Xu, C., Atmospheric oxidation mechanism of benzene. Fates of alkoxy radical intermediates and revised mechanism. *The journal of physical chemistry. A* **2013,** *117*, (51), 14163-8.

27. Wang, M.; Chen, D.; Xiao, M.; Ye, Q.; Stolzenburg, D.; Hofbauer, V.; Ye, P.; Vogel, A. L.; Mauldin, R. L., 3rd; Amorim, A.; Baccarini, A.; Baumgartner, B.; Brilke, S.; Dada, L.; Dias, A.; Duplissy, J.; Finkenzeller, H.; Garmash, O.; He, X. C.; Hoyle, C. R.; Kim, C.; Kvashnin, A.; Lehtipalo, K.; Fischer, L.; Molteni, U.; Petaja, T.; Pospisilova, V.; Quelever, L. L. J.; Rissanen, M.; Simon, M.; Tauber, C.; Tome, A.; Wagner, A. C.; Weitz, L.; Volkamer, R.; Winkler, P. M.; Kirkby, J.; Worsnop, D. R.; Kulmala, M.; Baltensperger, U.; Dommen, J.; El-Haddad, I.; Donahue, N. M., Photo-oxidation of Aromatic Hydrocarbons Produces Low-Volatility Organic Compounds. *Environmental science & technology* **2020,** *54*, (13), 7911-7921.

28. Cheng, X.; Chen, Q.; Li, Y. J.; Zheng, Y.; Liao, K. R.; Huang, G. C., Highly oxygenated organic molecules produced by the oxidation of benzene and toluene in a wide range of OH exposure and NOx conditions. *Atmospheric Chemistry and Physics* **2021,** *21*, (15), 12005-12019.

29. Xu, L.; Moller, K. H.; Crounse, J. D.; Kjaergaard, H. G.; Wennberg, P. O., New Insights into the Radical Chemistry and Product Distribution in the OH-Initiated Oxidation of Benzene. *Environmental science & technology* **2020,** *54*, (21), 13467-13477.

30. Garmash, O.; Rissanen, M. P.; Pullinen, I.; Schmitt, S.; Kausiala, O.; Tillmann, R.; Zhao, D. F.; Percival, C.; Bannan, T. J.; Priestley, M.; Hallquist, A. M.; Kleist, E.; Kiendler-Scharr, A.; Hallquist, M.; Berndt, T.; McFiggans, G.; Wildt, J.; Mentel, T.; Ehn, M., Multi-generation OH oxidation as a source for highly oxygenated organic molecules from aromatics. *Atmospheric Chemistry and Physics* **2020,** *20*, (1), 515-537.

31. Luo, H.; Vereecken, L.; Shen, H.; Kang, S.; Pullinen, I.; Hallquist, M.; Fuchs, H.; Wahner, A.; Kiendler-Scharr, A.; Mentel, T. F.; Zhao, D., Formation of highly oxygenated organic molecules from the oxidation of limonene by OH radical: significant contribution of H-abstraction pathway. *Atmos. Chem. Phys. Discuss.* **2022,** *2022*, 1-23.

32. Wang, Z.; Ehn, M.; Rissanen, M. P.; Garmash, O.; Quelever, L.; Xing, L.; Monge-Palacios, M.; Rantala, P.; Donahue, N. M.; Berndt, T.; Sarathy, S. M., Efficient alkane oxidation under combustion engine and atmospheric conditions. *Commun Chem* **2021,** *4*, (1), 18.

33. Zhu, M.; Wang, S. A.; Zhang, Y. L.; Yu, Z. Q.; Yu, Y. J.; Wang, X. M., Particle-Bound Highly Oxidized Organic Molecules Derived from Aromatic Hydrocarbons in an Urban Atmosphere. *Environmental science & technology* **2022,** *9*, (12), 1030-1036.

34. Frege, C.; Ortega, I. K.; Rissanen, M. P.; Praplan, A. P.; Steiner, G.; Heinritzi, M.; Ahonen, L.; Amorim, A.; Bernhammer, A. K.; Bianchi, F.; Brilke, S.; Breitenlechner, M.; Dada, L.; Dias, A.; Duplissy, J.; Ehrhart, S.; El-Haddad, I.; Fischer, L.; Fuchs, C.; Garmash, O.; Gonin, M.; Hansel, A.; Hoyle, C. R.; Jokinen, T.; Junninen, H.; Kirkby, J.; Kurten, A.; Lehtipalo, K.; Leiminger, M.; Mauldin, R. L.; Molteni, U.; Nichman, L.; Petaja, T.; Sarnela, N.; Schobesberger, S.; Simon, M.; Sipila, M.; Stolzenburg, D.; Tome, A.; Vogel, A. L.; Wagner, A. C.; Wagner, R.; Xiao, M.; Yan, C.; Ye, P. L.; Curtius, J.; Donahue, N. M.; Flagan, R. C.; Kulmala, M.; Worsnop, D. R.; Winkler, P. M.; Dommen, J.; Baltensperger, U., Influence of temperature on the molecular composition of ions and charged clusters during pure biogenic nucleation. *Atmospheric Chemistry and Physics* **2018,** *18*, (1), 65-79.

35. Stolzenburg, D.; Fischer, L.; Vogel, A. L.; Heinritzi, M.; Schervish, M.; Simon, M.; Wagner, A. C.; Dada, L.; Ahonen, L. R.; Amorim, A.; Baccarini, A.; Bauer, P. S.; Baumgartner, B.; Bergen, A.; Bianchi, F.; Breitenlechner, M.; Brilke, S.; Buenrostro Mazon, S.; Chen, D.; Dias, A.; Draper, D. C.; Duplissy, J.; El Haddad, I.; Finkenzeller, H.; Frege, C.; Fuchs, C.; Garmash, O.; Gordon,

H.; He, X.; Helm, J.; Hofbauer, V.; Hoyle, C. R.; Kim, C.; Kirkby, J.; Kontkanen, J.; Kurten, A.; Lampilahti, J.; Lawler, M.; Lehtipalo, K.; Leiminger, M.; Mai, H.; Mathot, S.; Mentler, B.; Molteni, U.; Nie, W.; Nieminen, T.; Nowak, J. B.; Ojdanic, A.; Onnela, A.; Passananti, M.; Petaja, T.; Quelever, L. L. J.; Rissanen, M. P.; Sarnela, N.; Schallhart, S.; Tauber, C.; Tome, A.; Wagner, R.; Wang, M.; Weitz, L.; Wimmer, D.; Xiao, M.; Yan, C.; Ye, P.; Zha, Q.; Baltensperger, U.; Curtius, J.; Dommen, J.; Flagan, R. C.; Kulmala, M.; Smith, J. N.; Worsnop, D. R.; Hansel, A.; Donahue, N. M.; Winkler, P. M., Rapid growth of organic aerosol nanoparticles over a wide tropospheric temperature range. *Proceedings of the National Academy of Sciences of the United States of America* **2018,** *115*, (37), 9122-9127.

36. Guo, Y. S.; Yan, C.; Liu, Y. L.; Qiao, X. H.; Zheng, F. X.; Zhang, Y.; Zhou, Y.; Li, C.; Fan, X. L.; Lin, Z. H.; Feng, Z. M.; Zhang, Y. S.; Zheng, P. G.; Tian, L. H.; Nie, W.; Wang, Z.; Huang, D. D.; Daellenbach, K. R.; Yao, L.; Dada, L.; Bianchi, F.; Jiang, J. K.; Liu, Y. C.; Kerminen, V. M.; Kulmala, M., Seasonal variation in oxygenated organic molecules in urban Beijing and their contribution to secondary organic aerosol. *Atmospheric Chemistry and Physics* **2022,** *22*, (15), 10077-10097.

37. Wu, A.; Knight, R.; Patin, J.; Herron, J. M.; DeGroot, B.; Ng, J. K.; Laskin, O. L., Coadministration of lenalidomide has no clinical significant effect on the pharmacokinetics of digoxin. *Clinical Pharmacology & Therapeutics* **2007,** *81*, (19), S40-S41.

38. Pye, H. O. T.; D'Ambro, E. L.; Lee, B. H.; Schobesberger, S.; Takeuchi, M.; Zhao, Y.; Lopez-Hilfiker, F.; Liu, J.; Shilling, J. E.; Xing, J.; Mathur, R.; Middlebrook, A. M.; Liao, J.; Welti, A.; Graus, M.; Warneke, C.; de Gouw, J. A.; Holloway, J. S.; Ryerson, T. B.; Pollack, I. B.; Thornton, J. A., Anthropogenic enhancements to production of highly oxygenated molecules from autoxidation. *Proceedings of the National Academy of Sciences of the United States of America* **2019,** *116*, (14), 6641-6646.

39. Sarrafzadeh, M.; Wildt, J.; Pullinen, I.; Springer, M.; Kleist, E.; Tillmann, R.; Schmitt, S. H.; Wu, C.; Mentel, T. F.; Zhao, D.; Hastie, D. R.; Kiendler-Scharr, A., Impact of NOx and OH on secondary organic aerosol formation from a-pinene photooxidation. *Atmospheric Chemistry and Physics* **2016,** *16*, (17), 11237-11248.

40. Yan, C.; Nie, W.; Vogel, A. L.; Dada, L.; Lehtipalo, K.; Stolzenburg, D.; Wagner, R.; Rissanen, M. P.; Xiao, M.; Ahonen, L.; Fischer, L.; Rose, C.; Bianchi, F.; Gordon, H.; Simon, M.; Heinritzi, M.; Garmash, O.; Roldin, P.; Dias, A.; Ye, P.; Hofbauer, V.; Amorim, A.; Bauer, P. S.; Bergen, A.; Bernhammer, A. K.; Breitenlechner, M.; Brilke, S.; Buchholz, A.; Mazon, S. B.; Canagaratna, M. R.; Chen, X.; Ding, A.; Dommen, J.; Draper, D. C.; Duplissy, J.; Frege, C.; Heyn, C.; Guida, R.; Hakala, J.; Heikkinen, L.; Hoyle, C. R.; Jokinen, T.; Kangasluoma, J.; Kirkby, J.; Kontkanen, J.; Kurten, A.; Lawler, M. J.; Mai, H.; Mathot, S.; Mauldin, R. L., 3rd; Molteni, U.; Nichman, L.; Nieminen, T.; Nowak, J.; Ojdanic, A.; Onnela, A.; Pajunoja, A.; Petaja, T.; Piel, F.; Quelever, L. L. J.; Sarnela, N.; Schallhart, S.; Sengupta, K.; Sipila, M.; Tome, A.; Trostl, J.; Vaisanen, O.; Wagner, A. C.; Ylisirnio, A.; Zha, Q.; Baltensperger, U.; Carslaw, K. S.; Curtius, J.; Flagan, R. C.; Hansel, A.; Riipinen, I.; Smith, J. N.; Virtanen, A.; Winkler, P. M.; Donahue, N. M.; Kerminen, V. M.; Kulmala, M.; Ehn, M.; Worsnop, D. R., Size-dependent influence of NO(x) on the growth rates of organic aerosol particles. *Sci Adv* **2020,** *6*, (22), eaay4945.

41. Praske, E.; Otkjaer, R. V.; Crounse, J. D.; Hethcox, J. C.; Stoltz, B. M.; Kjaergaard, H. G.; Wennberg, P. O., Atmospheric autoxidation is increasingly important in urban and suburban North America. *Proceedings of the National Academy of Sciences of the United States of America* **2018,**

115, (1), 64-69.

42. Tian, L.; Huang, D. D.; Li, Y. J.; Yan, C.; Nie, W.; Wang, Z.; Wang, Q.; Qiao, L.; Zhou, M.; Zhu, S.; Liu, Y.; Guo, Y.; Qiao, X.; Zheng, P.; Jing, S. a.; Lou, S.; Wang, H.; Huang, C., Enigma of Urban Gaseous Oxygenated Organic Molecules: Precursor Type, Role of NOx, and Degree of Oxygenation. *Environmental science & technology* **2023,** *57*, (1), 64-75.

43. Kurten, T.; Moller, K. H.; Nguyen, T. B.; Schwantes, R. H.; Misztal, P. K.; Su, L.; Wennberg, P. O.; Fry, J. L.; Kjaergaard, H. G., Alkoxy Radical Bond Scissions Explain the Anomalously Low Secondary Organic Aerosol and Organonitrate Yields From alpha-Pinene + NO(3). *J Phys Chem Lett* **2017,** *8*, (13), 2826-2834.

44. Yan, C.; Nie, W.; Aijala, M.; Rissanen, M. P.; Canagaratna, M. R.; Massoli, P.; Junninen, H.; Jokinen, T.; Sarnela, N.; Hame, S. A. K.; Schobesberger, S.; Canonaco, F.; Yao, L.; Prevot, A. S. H.; Petaja, T.; Kulmala, M.; Sipila, M.; Worsnop, D. R.; Ehn, M., Source characterization of highly oxidized multifunctional compounds in a boreal forest environment using positive matrix factorization. *Atmospheric Chemistry and Physics* **2016,** *16*, (19), 12715-12731.

45. Chen, Y.; Zheng, P.; Wang, Z.; Pu, W.; Tan, Y.; Yu, C.; Xia, M.; Wang, W.; Guo, J.; Huang, D.; Yan, C.; Nie, W.; Ling, Z.; Chen, Q.; Lee, S.; Wang, T., Secondary Formation and Impacts of Gaseous Nitro-Phenolic Compounds in the Continental Outflow Observed at a Background Site in South China. *Environmental science & technology* **2022,** *56*, (11), 6933-6943.

46. Zhang, Y.; Perakyla, O.; Yan, C.; Heikkinen, L.; Äijälä, M.; Daellenbach, K.; Zha, Q.; Riva, M.; Garmash, O.; Junninen, H.; Paatero, P.; Worsnop, D.; Ehn, M., *A Novel Approach for Simple Statistical Analysis of High-Resolution Mass Spectra*. 2019; p 1-32.

47. Heinritzi, M.; Simon, M.; Steiner, G.; Wagner, A. C.; Kurten, A.; Hansel, A.; Curtius, J., Characterization of the mass-dependent transmission efficiency of a CIMS. *Atmospheric Measurement Techniques* **2016,** *9*, (4), 1449-1460.

48. Berndt, T.; Richters, S.; Kaethner, R.; Voigtlander, J.; Stratmann, F.; Sipila, M.; Kulmala, M.; Herrmann, H., Gas-Phase Ozonolysis of Cycloalkenes: Formation of Highly Oxidized RO2 Radicals and Their Reactions with NO, NO2, SO2, and Other RO2 Radicals. *The journal of physical chemistry. A* **2015,** *119*, (41), 10336-48.

49. Paatero, P.; Tapper, U., Positive matrix factorization: A non-negative factor model with optimal utilization of error estimates of data values. *Environmetrics* **1994,** *5*, (2), 111-126.

50. Paatero, P., User's Guide for Positive Matrix Factorization programs PMF2 and PMF3. **2004,** *Parts 1 and 2*.

51. Ulbrich, I. M.; Canagaratna, M. R.; Zhang, Q.; Worsnop, D. R.; Jimenez, J. L., Interpretation of organic components from Positive Matrix Factorization of aerosol mass spectrometric data. *Atmospheric Chemistry and Physics* **2009,** *9*, (9), 2891-2918.

52. Donahue, N. M.; Epstein, S. A.; Pandis, S. N.; Robinson, A. L., A two-dimensional volatility basis set: 1. organic-aerosol mixing thermodynamics. *Atmospheric Chemistry and Physics* **2011,** *11*, (7), 3303-3318.

53. Pankow, J. F.; Asher, W. E., SIMPOL.1: a simple group contribution method for predicting vapor pressures and enthalpies of vaporization of multifunctional organic compounds. *Atmospheric Chemistry and Physics* **2008,** *8*, (10), 2773-2796.

54. Trostl, J.; Chuang, W. K.; Gordon, H.; Heinritzi, M.; Yan, C.; Molteni, U.; Ahlm, L.; Frege, C.; Bianchi, F.; Wagner, R.; Simon, M.; Lehtipalo, K.; Williamson, C.; Craven, J. S.; Duplissy, J.; Adamov, A.; Almeida, J.; Bernhammer, A. K.; Breitenlechner, M.; Brilke, S.; Dias, A.; Ehrhart, S.; Flagan, R. C.; Franchin, A.; Fuchs, C.; Guida, R.; Gysel, M.; Hansel, A.; Hoyle, C. R.; Jokinen, T.; Junninen, H.; Kangasluoma, J.; Keskinen, H.; Kim, J.; Krapf, M.; Kurten, A.; Laaksonen, A.; Lawler, M.; Leiminger, M.; Mathot, S.; Mohler, O.; Nieminen, T.; Onnela, A.; Petaja, T.; Piel, F. M.; Miettinen, P.; Rissanen, M. P.; Rondo, L.; Sarnela, N.; Schobesberger, S.; Sengupta, K.; Sipila, M.; Smith, J. N.; Steiner, G.; Tome, A.; Virtanen, A.; Wagner, A. C.; Weingartner, E.; Wimmer, D.; Winkler, P. M.; Ye, P.; Carslaw, K. S.; Curtius, J.; Dommen, J.; Kirkby, J.; Kulmala, M.; Riipinen, I.; Worsnop, D. R.; Donahue, N. M.; Baltensperger, U., The role of low-volatility organic compounds in initial particle growth in the atmosphere. *Nature* **2016,** *533*, (7604), 527-31.

55. Seinfeld, J. H. and Pandis, S, N., *Atmospheric chemistry and physics : from air pollution to climate change*. Third edition.. ed.; Hoboken, New Jersey : Wiley: Hoboken, New Jersey, 2016; p 584.

56. Bianchi, F.; Garmash, O.; He, X.; Yan, C.; Iyer, S.; Rosendahl, I.; Xu, Z.; Rissanen, M. P.; Riva, M.; Taipale, R.; Sarnela, N.; Petäjä, T.; Worsnop, D. R.; Kulmala, M.; Ehn, M.; Junninen, H., The role of highly oxygenated molecules (HOMs) in determining the composition of ambient ions in the boreal forest. *Atmos. Chem. Phys.* **2017,** *17*, (22), 13819-13831.

57. Isokääntä, S.; Mikkonen, S.; Laurikainen, M.; Buchholz, A.; Schobesberger, S.; Blande, J. D.; Nieminen, T.; Ylivinkka, I.; Bäck, J.; Petäjä, T.; Kulmala, M.; Yli-Juuti, T., Multivariate model-based investigation of the temperature dependence of ozone concentration in Finnish boreal forest. *Atmospheric Environment* **2022,** *289*, 119315.

58. Kroll, J. H.; Donahue, N. M.; Jimenez, J. L.; Kessler, S. H.; Canagaratna, M. R.; Wilson, K. R.; Altieri, K. E.; Mazzoleni, L. R.; Wozniak, A. S.; Bluhm, H.; Mysak, E. R.; Smith, J. D.; Kolb, C. E.; Worsnop, D. R., Carbon oxidation state as a metric for describing the chemistry of atmospheric organic aerosol. *Nat Chem* **2011,** *3*, (2), 133-9.

59. Zha, Q. Z.; Yan, C.; Junninen, H.; Riva, M.; Sarnela, N.; Aalto, J.; Quelever, L.; Schallhart, S.; Dada, L.; Heikkinen, L.; Perakyla, O.; Zou, J.; Rose, C.; Wang, Y. H.; Mammarella, I.; Katul, G.; Vesala, T.; Worsnop, D. R.; Kulmala, M.; Petaja, T.; Bianchi, F.; Ehn, M., Vertical characterization of highly oxygenated molecules (HOMs) below and above a boreal forest canopy. *Atmospheric Chemistry and Physics* **2018,** *18*, (23), 17437-17450.

60. Zhou, S.; Wang, T.; Wang, Z.; Li, W.; Xu, Z.; Wang, X.; Yuan, C.; Poon, C. N.; Louie, P. K. K.; Luk, C. W. Y.; Wang, W., Photochemical evolution of organic aerosols observed in urban plumes from Hong Kong and the Pearl River Delta of China. *Atmospheric Environment* **2014,** *88*, 219-229.

61. Brean, J.; Harrison, R. M.; Shi, Z. B.; Beddows, D. C. S.; Acton, W. J. F.; Hewitt, C. N.; Squires, F. A.; Lee, J., Observations of highly oxidized molecules and particle nucleation in the atmosphere of Beijing. *Atmospheric Chemistry and Physics* **2019,** *19*, (23), 14933-14947.

62. Ye, Q.; Wang, M.; Hofbauer, V.; Stolzenburg, D.; Chen, D.; Schervish, M.; Vogel, A.; Mauldin, R. L.; Baalbaki, R.; Brilke, S.; Dada, L.; Dias, A.; Duplissy, J.; El Haddad, I.; Finkenzeller, H.; Fischer, L.; He, X.; Kim, C.; Kurten, A.; Lamkaddam, H.; Lee, C. P.; Lehtipalo, K.; Leiminger, M.; Manninen, H. E.; Marten, R.; Mentler, B.; Partoll, E.; Petaja, T.; Rissanen, M.; Schobesberger, S.; Schuchmann, S.; Simon, M.; Tham, Y. J.; Vazquez-Pufleau, M.; Wagner, A. C.; Wang, Y.; Wu, Y.;

834 Xiao, M.; Baltensperger, U.; Curtius, J.; Flagan, R.; Kirkby, J.; Kulmala, M.; Volkamer, R.; Winkler,
835 P. M.; Worsnop, D.; Donahue, N. M., Molecular Composition and Volatility of Nucleated Particles
836 from alpha-Pinene Oxidation between -50 degrees C and +25 degrees C. *Environmental science*
837 *& technology* **2019,** *53*, (21), 12357-12365.

838 63. Li, H. Y.; Riva, M.; Rantala, P.; Heikkinen, L.; Daellenbach, K.; Krechmer, J. E.; Flaud, P. M.;
839 Worsnop, D.; Kulmala, M.; Villenave, E.; Perraudin, E.; Ehn, M.; Bianchi, F., Terpenes and their
840 oxidation products in the French Landes forest: insights from Vocus PTR-TOF measurements.
841 *Atmospheric Chemistry and Physics* **2020,** *20*, (4), 1941-1959.

842 64. Draper, D. C.; Myllys, N.; Hyttinen, N.; Moller, K. H.; Kjaergaard, H. G.; Fry, J. L.; Smith, J.
843 N.; Kurten, T., Formation of Highly Oxidized Molecules from NO3 Radical Initiated Oxidation of
844 Delta-3-Carene: A Mechanistic Study. *Acs Earth and Space Chemistry* **2019,** *3*, (8), 1460-1470.

845 65. Riva, M.; Ehn, M.; Li, D.; Tomaz, S.; Bourgain, F.; Perrier, S.; George, C., CI-Orbitrap: An
846 Analytical Instrument To Study Atmospheric Reactive Organic Species. *Anal Chem* **2019,** *91*, (15),
847 9419-9423.

848 66. Riba, M. L.; Tathy, J. P.; Tsiropoulos, N.; Monsarrat, B.; Torres, L., Diurnal variation in the
849 concentration of α- and β-pinene in the landes forest (France). *Atmospheric Environment (1967)*
850 **1987,** *21*, (1), 191-193.

851 67. Bianchi, F.; Garmash, O.; He, X.; Yan, C.; Iyer, S.; Rosendahl, I.; Xu, Z.; Rissanen, M. P.;
852 Riva, M.; Taipale, R.; Sarnela, N.; Petäjä, T.; Worsnop, D. R.; Kulmala, M.; Ehn, M.; Junninen,
853 H., The role of highly oxygenated molecules (HOMs) in determining the composition of ambient
854 ions in the boreal forest. *Atmos. Chem. Phys.* **2017,** *17*, (22), 13819-13831.

855 68. Ehn, M.; Junninen, H.; Petäjä, T.; Kurtén, T.; Kerminen, V. M.; Schobesberger, S.; Manninen,
856 H. E.; Ortega, I. K.; Vehkamäki, H.; Kulmala, M.; Worsnop, D. R., Composition and temporal
857 behavior of ambient ions in the boreal forest. *Atmos. Chem. Phys.* **2010,** *10*, (17), 8513-8530.

858 69. Huang, W.; Li, H.; Sarnela, N.; Heikkinen, L.; Tham, Y. J.; Mikkilä, J.; Thomas, S. J.; Donahue,
859 N. M.; Kulmala, M.; Bianchi, F., Measurement report: Molecular composition and volatility of
860 gaseous organic compounds in a boreal forest – from volatile organic compounds to highly
861 oxygenated organic molecules. *Atmos. Chem. Phys.* **2021,** *21*, (11), 8961-8977.

862

Supplemental information for:

Molecular characterization of oxygenated organic molecules and their dominating roles in particle growth in Hong Kong

*Penggang Zheng [1,2], Yi Chen [1,2], Zhe Wang [1, *], Yuliang Liu [3], Wei Pu [2], Chuan Yu [2], Men Xia [2], Yang Xu [1], Jia Guo [4], Yishuo Guo [5], Linhui Tian [6], Xiaohui Qiao [7], Dan Dan Huang [8], Chao Yan [3,9], Wei Nie [3], Douglas R. Worsnop [9, 10], Shuncheng Lee [2], Tao Wang [2]*

[1] Division of Environment and Sustainability, The Hong Kong University of Science and Technology, Hong Kong SAR 999077, China

[2] Department of Civil and Environmental Engineering, The Hong Kong Polytechnic University, Hong Kong SAR 999077, China

[3] Joint International Research Laboratory of Atmospheric and Earth System Research, School of Atmospheric Sciences, Nanjing University, Nanjing 210023, China

[4] Environmental Central Facility, The Hong Kong University of Science and Technology, Hong Kong SAR 999077, China

[5] Aerosol and Haze Laboratory, Beijing Advanced Innovation Center for Soft Matter Science and Engineering, Beijing University of Chemical Technology, Beijing 100084, China

[6] Department of Civil and Environmental Engineering, Faculty of Science and Technology, University of Macau, Taipa, Macau 999078, China.

[7] State Key Joint Laboratory of Environment Simulation and Pollution Control, School of Environment, Tsinghua University, Beijing 100084, China

[8] State Environmental Protection Key Laboratory of Formation and Prevention of Urban Air Pollution Complex, Shanghai Academy of Environmental Sciences, Shanghai 200233, China

[9] Institute for Atmospheric and Earth System Research / Physics, Faculty of Science, University of Helsinki 00014, Finland

[10] Aerodyne Research Inc., Billerica, MA 01821, USA.

The supplement contains supporting texts, 17 figures and 6 tables, in total 36 pages.

ToF-CIMS settings, calibration and transmission

Settings: The nitrate-based Tof-CIMS (Aerodyne Research) was used to measure the OOMs in this study. The instrument consists of a time-of-flight mass spectrometer coupled to a chemical ionization source which ionizes sampled molecules with nitric acid[1]. Detailed description of the instrument can be found in our previous studies[2, 3]. Briefly, the ambient air was sampled to the instrument with a flowrate of 10LPM through a 2.5m long stainless-steel inlet. Then, the sampled molecules will be ionized in the ion-molecule reaction (IMR) chamber by the nitrate cluster ions in the sheath flow, which consists of purified airflow (20L/min) and nitric acid stream (5ml/min). The reagent ions of nitrate cluster were produced by irradiation with a PhotoIonizer X-Ray (Model L9491, Hamamatsu, Japan). Finally, the ionized OOMs would be extracted into the ToF and determined based on the flight times in the mass spectrometer.

Calibration: Sensitivity calibration was performed with sulfuric acid by following the method developed by Kürten et al..[4] Briefly, a known concentration of OH radicals is generated from the photolysis of water with a 185 nm UV lamp, and then reacts with excessive SO_2 to produce the sulfuric acid standard gas to fed into the inlet of Tof-CIMS. The calibration coefficient is obtained as follows,

$$[H_2SO_4] = C_{H_2SO_4} \times SL_{H_2SO_4} \times \ln\left(1 + \frac{[HSO_4^-] + [HSO_4^- \cdot HNO_3]}{\sum_{n=0}^{2}[NO_3^- \cdot (HNO_3)_n]}\right) \quad (1)$$

where $[H_2SO_4]$ is the concentration of sulfuric acid standard gas. Species in the brackets are the concentrations of primary ions and target ions detected by the ToF-CIMS. [2, 3] The calibration factor considering the inlet diffusion loss, ($C_{H2SO4} \times SL_{H2SO4}$) is determined to be 9.88×10^{-9} molecule cm^{-3} in this study. Due to the unknown structures and unavailable standard substances of detected OOMs, the calibration factor of sulfuric acid was also applied to OOMs,

by assuming a similar ionization efficiency as suggested by previous studies[5].

Transmission: As mass discrimination effect highly affects CIMS quantification, the perfluorinated heptanoic acid with high electronegativity[6], was used to obtain the mass-dependent transmission efficiency of the instrument. Based on the conservation relationship of consumed primary ions and charged monomer, dimer and trimer of perfluorinated heptanoic acid, the transmission efficiency of the instrument is fitted as follow,

$$T_i = 0.0022 + 1.01 \times e^{-\left(\frac{m_i - 114.08}{366.18}\right)^2} \quad (2)$$

where T is the mass-dependent transmission efficiency and m is the mass of the detected ions.

Finally, the OOMs concentration is derived from the following equation after taking account of both transmission efficiency and calibration coefficient.

$$[OOM_i] = C_{H_2SO_4} \times \frac{1}{T_i} \times \ln\left(1 + \frac{\sum_{n=0}^{1}[OOM_i \cdot (HNO_3)_n \cdot NO_3 + HNO_3 \cdot (OOM_i - H)^-]}{\sum_{n=0}^{2}[NO_3^- \cdot (HNO_3)_n]}\right) \quad (3)$$

Positive matrix factorization

PMF model settings: Positive matrix factorization (PMF) is a powerful analysis method to extract sources of pollutants with different time evolution.[7] The model establishes a mass-balance among a $m \times n$ data matrix X and factors time series G, factor profiles F, and residue matrix E, as described in the formula below,

$$X_{i,j} = \sum_p G_{i,p} F_{p,j} + E_{i,j} \quad (4)$$

where i and j refer to the indices of the row and column of the data matrix, respectively. p is the factor solution. Using the least-square algorithm, the model runs to seek the minimum Q, defined as

$$Q = \sum_{i=1}^{m}\sum_{j=1}^{n}(\frac{E_{i,j}}{\sigma_{i,j}})^2 \quad (5)$$

where σ is the error estimation of the data matrix.

With the focus on the OOMs species, some unrelated and unconcerned peaks are excluded from the prepared PMF data matrix, including nitrophenols, contaminations, chlorides, bromides, iodides and sulfides. The presence of high concentrations of nitrophenols may dominate the PMF results. Thus, considering the distinct properties of the nitrophenols, they were studied separately in our previous work[2] and are excluded from following analysis in this study. Fluorinated contaminations emitted from tubing are also removed. The chlorides, bromides, iodides and sulfides are not the concerned species in this study and are also excluded from the data matrix. The formulas of the excluded species are listed in Table S5. In addition, the missing values in the data matrix are replaced with 5th percentile of the corresponding species.

The uncertainties of OOMs data and error estimation are crucial for the PMF analysis. The error matrix is estimated from the method suggested by Yan et al. [8], as follow,

$$S_{i,j} = \sigma_{i,j} + \sigma_{noise} = a\frac{\sqrt{I}}{\sqrt{t}} + \sigma_{noise} \quad (6)$$

where $\sigma_{i,j}$ is the uncertainties resulted from counting statistics and is related to data integration time t and signal strength I. The $\sigma_{i,j}$ is further corrected with an experiment obtained empirically constant a (1.28)[8]. σ_{noise} is the standard deviation of the instrument noise and is calculated as 0.035 according to laboratory result of Yan et al.[8].

PMF solution diagnostics:

Choosing the proper factors solution is the most critical step to interpret the PMF result. The evolution of PMF solutions is examined to facilitate the choosing of optimized factors. A total

of 3 to 20 factors are iterated with the PMF model, and the interpretation for the solution evolution of first 9 factors are summarized in Table S6. In the initial solution with three factors, an obvious CHO, CHON and CHON2 factors are observed according to their fingerprint peaks. In the four-factor solution, a night-time factor emerges and is identified as monoterpene and isoprene mixed factor for the presence of C5 and C10 fingerprint peaks. With the evolution of the solutions, the CHON and CHO factors are further separated in the five-factor and six-factor solutions, and the four-oxygen (O4), O5, O6 with 1N, O7 with 1N, monoterpene and isoprene mixed (MT, iso mixed), and 2N factors are obtained. Although more factors allow the model to explain more OOMs, it also may force the model to split the physically meaningful factor into unrealistic factors[8]. When the solution is pushed to seven-factor, a O6 with 2N factor is split from previous 1NO6 and 2N factors. Generally, the CHON and CHON2 OOMs are different generation products. Their combination may imply the over-split in seven-factor solution. In the evolution of higher solutions, more over-split factors identified as unrealistic factors as shown in the profiles. Thus, from the perspective of PMF solution evolution, the six-factor are most suitable solution, with the richest profiles and the least over-split.

Besides the solution evolution analysis, the values of Q/Q_{exp} and max rotational matrix (RotMat) are another two important metrics to mathematically evaluate the solution.[9] The Q is the sum of squared, scaled residuals and Q_{exp} is the expected mean value of Q. The PMF2 uses the least squares method to solve the bilinear model, and Q therefore follows the chi-square distribution and its degrees of freedom equals to the Q_{exp}, which is given by[10],

$$Q_{exp} = m \cdot n - p \cdot (m + n) \quad (7)$$

where p is number of factors, m and n are the row and column number of data matrix X, respectively. For a CIMS dataset, $m \times n >> p(m+n)$, so $Q_{exp} \approx m \times n$. As the residuals of the

bilinear model, the Q generally shows a decrease trend in the solutions iteration as additional factors would fit more of data. Furthermore, the sharp drop of Q implies that the additional factor explained the data significantly and is often treated as a sign to determine the solutions[7]. The max RotMat represents the highest rotational freedom case in a solution, and the high value points should be rejected for its large rotational ambiguity[11].

The Q/Q_{exp} and max RotMax variation over solutions from 3 to 20 is shown in Figure S16 Mathematical diagnostics of PMF solutions, including values of Q/Qexp, the maximum value of rotation matrix (RotMat) versus the number of factors (Fpeak=0), and explained fraction of each solution. (Fpeak=0). The model doesn't have the solution for 9, 10, 14, 15, 16, 17 factors. For the rest solutions, the Q/Q_{exp} shows a decrease trend, ranging from 3 to 7. The high absolute values suggest the uncertainties of the data could be underestimated due to the different instrument configuration compared to Yan et al.[8], and the Q/Q_{exp} trend should be more meaningful to determine the minimum factor number. A large drop of Q/Q_{exp} on 3 to 4 factors and clear increase of explained data variation from 90 to 93% indicate that at least four factors are needed to explain the data. The 10, 14 and 16 factors exhibit a rapid max RotMat increase and are thus rejected from further analysis. Combined with previous solution evolution analysis, the six-factor are finally chosen as a better solution with 93.9% of data explained.

For a certain factors solution, the solution matrix (G and F) is not unique due to the existence of linear transformations of factor time series and factor profiles, such that,

$$GF = GTT^{-1}F \quad (8)$$

where T is a transformation matrix and T^{-1} is its inverse. The influence of the multiple solutions is called the rotational ambiguity[10]. In PMF2, once the best number of factors is determined, a subset of possible solutions is explored via different Fpeak. The Figure S17a shows the Q/Q_{exp}

variation over Fpeak from -1 to 1 for 6 factors solution[12]. The model doesn't have the solution for Fpeak of -1, -0.8 and 1. For the rest Fpeak, their Q/Q_{exp} values almost keep constant, ranging from 5.14 to 5.16, which implies the rotational ambiguity for six-factor solution is negligible. The factors time series and profiles of different Fpeak are also compared and show minor difference. Finally, the Fpeak of 0 was chosen as the solution. For the six factors solutions, six seed runs ranging from 0 to 20 with an interval of 4 were also performed to test the consistency of the solution and the result is shown in Figure S17b. The model doesn't have the solution for seed run of 8. For the rest seeds run, they show good consistencies in both Q/Qexp (5.14-5.16) and explained variation (93.9%-94.1%), indicating the small model uncertainty.

OOMs carbon oxidation state (OSc) and volatility estimation

The carbon oxidation state (OS_c) is an ideal metric to quantify the oxidation degree of organic species in the atmosphere and is defined as follows,

$$OS_c = -\sum_i OS_i \frac{n_i}{n_C} \quad (9)$$

Where OS_i is the oxidation state associated with element i, and n_i/nC is the molar ratio of element i to carbon. Based on the categorization scheme, the identified OOMs (except terpenes) OSc were calculated with their functional groups and carbon numbers. A group OSc oxidation state of −1 was used for -OH, -OOH, $-ONO_2$, $-OONO_2$, and $-NO_2$ groups, and a group OSc oxidation state of −2 was used for carbonyls group.

For terpene-derived OOMs and unidentified OOMs, their OSc were calculated following Massoli et al. from eq 1.

$$OS_c = 2 \times \frac{n_O}{n_c} - \frac{n_H}{n_c} - 5 \times \frac{n_N}{n_c} \quad (10)$$

where n_O, n_C, n_N and n_H are the numbers of elements in the OOMs formulas.

Volatility is an important parameter to reflect the ability of OOMs to condense/partition on particle phase. In previous studies[3, 13-15], the semi-theoretical parameterization method developed by Donahue et al[13]. was widely used to evaluate the OOMs volatility, which assumes that the majority anthropogenic OOMs consists of multifunctional groups including organic acid terminal and an even combination of hydroxyl and carbonyls along the backbone, and nitrate groups, as below.

$$log_{10}C^*(300K) = (25 - nC) \cdot bC - (nO - 2nN) \cdot bO - 2 * \left[\frac{(nO - 2nN) \cdot nC}{nC + nO - 2nN}\right] \cdot bCO \quad (11)$$

where nC, nO and nN are the numbers of carbon, oxygen, and nitrogen in OOMs formulas, with bC=0.475, bO=2.3, and bCO=-0.3.

Mohr et al. further improved the parameterization method to reflect the extensive of proxy groups (-OOH) in the monoterpene-OOMs produced from the autooxidation process[16], as follows:

$$log_{10}C^*(300K) = (25 - nC) \cdot bC - (nO - 3nN) \cdot bO - 2 * \left[\frac{(nO - 3nN) \cdot nC}{nC + nO - 3nN}\right] \cdot bCO - nN \cdot bN \quad (12)$$

where bC=0.475, bO=0.2, bCO=0.9, and bN=2.5.

The functional groups contribution method (simplified p_L^o prediction method, SIMPOL.1) developed by Pankow et al.[17] is a more explicit theoretical method for predicting organic molecules volatility, but the application was limited for OOMs due to the lack of exact functional groups information. The method assumes that the organics volatility is determined by the linear combination of contributions from parent hydrocarbons and multiple functional groups. The logarithm value of the saturated vapor pressure (C_i^*) of compound *i* is defined by,

$$log_{10}C^*(300K) = (25 - nC) \cdot bC + \sum_k v_{k,i}\tau_k \quad (13)$$

where bC=0.475, and $v_{k,i}$ is the number of groups of type k in i, τ_k is the group contribution term for group k and is given in Table S4. In the present study, the Mohr and SIMPOL.1 methods are used to estimate the volatility of monoterpene-OOMs and those OOMS with identified functional groups respectively, while Donahue's method was used for other detected OOMs. In addition, the OOMs volatility at ambient temperature is obtained by correcting the temperature effect[3] with equations below,

$$log_{10}C^*(T) = log_{10}C^*(300K) + \frac{\Delta H_{vap}}{Rln(10)}(\frac{1}{300} - \frac{1}{T}) \quad 14$$

in which, the evaporation enthalpy ΔH_{vap} is obtained with following equation.

$$\Delta H_{vap}[kJ\ mol^{-1}] = -5.7 \cdot log_{10}C^*(300K) + 129 \quad 15$$

Deduction of OOM functional groups for different categories

Both the termination functional groups and those functional groups formed in the reaction process should be considered in volatility estimation of OOMs. The multi-functional groups might consist of several combination ways. Based on PMF and mechanism analysis in section 3.3 in main text and Figure S8, Figure S9, Figure S10, Figure S11, here we assume that except di-nitrates and terpenes, other groups of OOMs were mostly first-generation products from hydrocarbon oxidation to simplify the structure information. OOMs structure are deduced and shown in Table S4. Specifically, besides the C=O group, the carbonyls with DBE of 3 are most likely the ring-opening products from aromatics and additionally contained one C=O, one C=C and two -OH groups (e.g., No.2 in Figure S15 formed via the pathway 5 in Figure S8). The carbonyls with DBE of 2 are considered as oxidation products from alkenes or alkanes and may additionally contain one C=C, one -OH group and at least one -OOH group (e.g., No.1 in Figure S15 formed via the pathway 1 in Figure S9). The hydroperoxides, nitrates and peroxyl nitrates

could contain at least one -OOH, one nitrate (-ONO_2) group, one peroxyl nitrate (-$OONO_2$) group, respectively. For those three categorizes, the OOMs with DBE of 3 are the ring-retaining oxidation products from aromatics and shall also contain one C=C, one -OH group, two non-aromatic rings (e.g., No. 5, 8, 11 in Figure S15 formed via pathway 2, 3, 4 in Figure S8, respectively); the species with DBE of 2 might be generated from aromatics oxidation as the ring-opening species with one more C=O, one more C=C, and two more -OH groups (e.g., No. 4, 7, 10 in Figure S15 formed via pathway 6, 7, 8 in Figure S8, respectively); the species with DBE of 1 might also contain one C=C, one -OH group and more than one -OOH groups (e.g., No. 2, 3, 4 in Figure S15 and formed via pathway of 2, 3, 4 in Figure S8). The remaining oxygen atoms in the OOM species are assumed to be presented as the -OOH group considering the efficient autoxidation processes in all types of OOMs formation. The ring-retaining species mainly referred to phenols and shall contain one aromatic ring, one nitro group (-NO_2) and one -OH group with remaining oxygen atoms evenly distributed between the -OH and -OOH groups (e.g., No. 12, 13 in Figure S15). The di-nitrates included two -ONO_2 groups with remaining oxygen atoms in -OH groups (e.g., No. 14, 15, 16 in Figure S15). The main functional groups of terpenes derived OOMs were -OOH and -ONO_2 groups as suggested by previous chamber studies (e.g., No. 17 in Figure S15)[14]. For those OOM molecules not classified into those groups will still follow the parameterization method assumptions.

Aerosol growth model

To calculate the OOMs mass flux onto the particles, an aerosol growth model developed by Tröstl et al.[14] is used to mathematically simulate the OOMs condensation process. The OOMs are firstly grouped into different volatility basis set (VBS) bins, where the saturation concentration of adjacent bins is ten times different[18]. The OOMs in every VBS bin are treated like single surrogate species having the properties of the averaged mass and concentration of

the OOMs in same bin. In the simulation model, the over-saturated part will condensate on the particles in the collide process, and the net mass flux can be calculated as,

$$\frac{dm_p}{dt} = \sigma_p \cdot k_p \cdot F_p \quad (16)$$

where $\sigma_{i,p}$ is the collision cross-section of particles and vapors, $k_{i,p}$ is the vapors deposition rate at the surface, and $F_{i,p}$ is the condensation driving force. $\sigma_{i,p}$ is calculated by $\sigma_{i,p} = \pi/4(d_p + d_i)^2$ with d_p the particle diameter and d_i the diameter of OOMs in VBS bins. $k_{i,p}$ is positively related to center mass velocity of particles and vapors ($v_{i,p}$) and is also corrected with the mass accommodation coefficient $\alpha_{i,p}$ and non-continuum dynamic factor $\beta_{i,p}$. The driving force is calculated as follows,

$$F_{i,p} = C_i^v - a'_{i,p} C_i^0 = C_i^v - X_{i,p}\gamma_{i,p}K_{i,p}C_i^0 \quad (17)$$

where C_i^v and C_i^0 are vapors ambient concentration and their saturation concentration, respectively. $a'_{i,p}$ is the activity of specie *i* at the particle phase surface, containing the Raoult term ($X_{i,p}\gamma_{i,p}$) and the Kelvin term ($K_{i,p}$) to account for the particles mixture effect and curvature effect respectively. In the Raoult term, $X_{i,p}$ is the condensed-phase mass fraction in a certain size particle, which is also the main source of uncertainty in the model calculation. $X_{i,p}$ cannot be measured directly due to the current technology limitations. Here, we adopt the values from chamber results of Tröstl et al. [14] and substitute the extreme $X_{i,p}$ values into all VBS bins to derive the lower and upper boundaries of model's uncertainties.

In addition, a parametrization method to estimate the growth rates of sulfuric acid was used following Stolzenburg et al.[19],

$$GR\ of\ SA(nm\ h^{-1}) = \left[2.73 * d_p(nm)^{-0.75} + 0.54\right] * \left[H_2SO_4(cm^{-3}) * 10^{-7}\right] \quad (18)$$

Gas-particles partitioning equation

Due to the high volatility, the SVOC in the gas and particle phases could quickly reach an equilibrium state through the gas-particle partitioning equation as follows [20],

$$f_i^s = \frac{1}{1 + \frac{C_i^*}{C_{OA}^s}} \quad (19)$$

where C_i^* is the vapors effective saturation concentration and C_{OA}^s is the concentration of organic aerosol. In this study, new particle formation (NPF) cases were selected, and the temporal evolution of the particle mobility diameter was compared with the simulated results to evaluate the OOMs contribution to the particles growth rate.

MCM inputs

The reaction mechanisms of pollutants were extracted from MCM 3.3.1 website (http://chmlin9.leeds.ac.uk/MCM/roots.htt), and the observed NO, NO_2, SO_2, O_3, CO, N_2O_5, RH, T, JNO_2, benzene, toluene, xylene/ethylbenzene, isoprene, propene, propane, butane, pentane, i-butane, i-pentane, particle nitrate, organic aerosol, and surface area of aerosol were input into the model every 10 minutes to constrain the simulation. The simulation period was from 8 November to 3 December and a 48-hour spin-up time was used in the MCM model. The simulated concentrations of OH, HO_2, and NO_3 radicals were output every minute. The average peak concentrations of OH and HO_2 radicals were 1.02×10^6 and 3.09×10^8 molecule cm^{-3} and peaked at 11:00 LT and 13:00 LT, respectively. NO_3 radical as a nocturnal oxidant showed the highest concentration of 1.70×10^8 molecule cm^{-3} at 20:00 LT. The detailed model description could be found in our previous studies.[2]

HYSPLIT model setting for footprint retroplume

To further estimate the influence of transportation and source regions on the observed OOMs, a footprint analysis was performed with a Lagrangian dispersion (HYSPLIT) model. The model setting is similar to a pervious study also conducted in Hok Tsui site[21]. The Kantha-Clayson scheme was used to compute vertical turbulence. In each simulation, 3000 particles were released at a height of 100m above the ground level at the site in an hour and backward in time for a 72h period. The position of released particles were calculated using a 3-D particle horizontal and vertical method every three hours during the campaign. The particle residence time within each vertical layer was calculated according to the particle spatial distribution. The simulated region was gridded with a spatial resolution of 0.1° in latitude by 0.1° in longitude; the domain covers 70° in longitude and 50° in latitude with the center located at the Hok Tsui station. Following a method developed by Stohl et al.[22] we calculated the residence time at 100m altitude to get a "footprint" retroplume of released air particles, which represents the distribution of probability or residence time of a simulated air mass. The footprint retroplumes shows consistent overall transport patterns with the cluster analysis of backward trajectories.

Figures

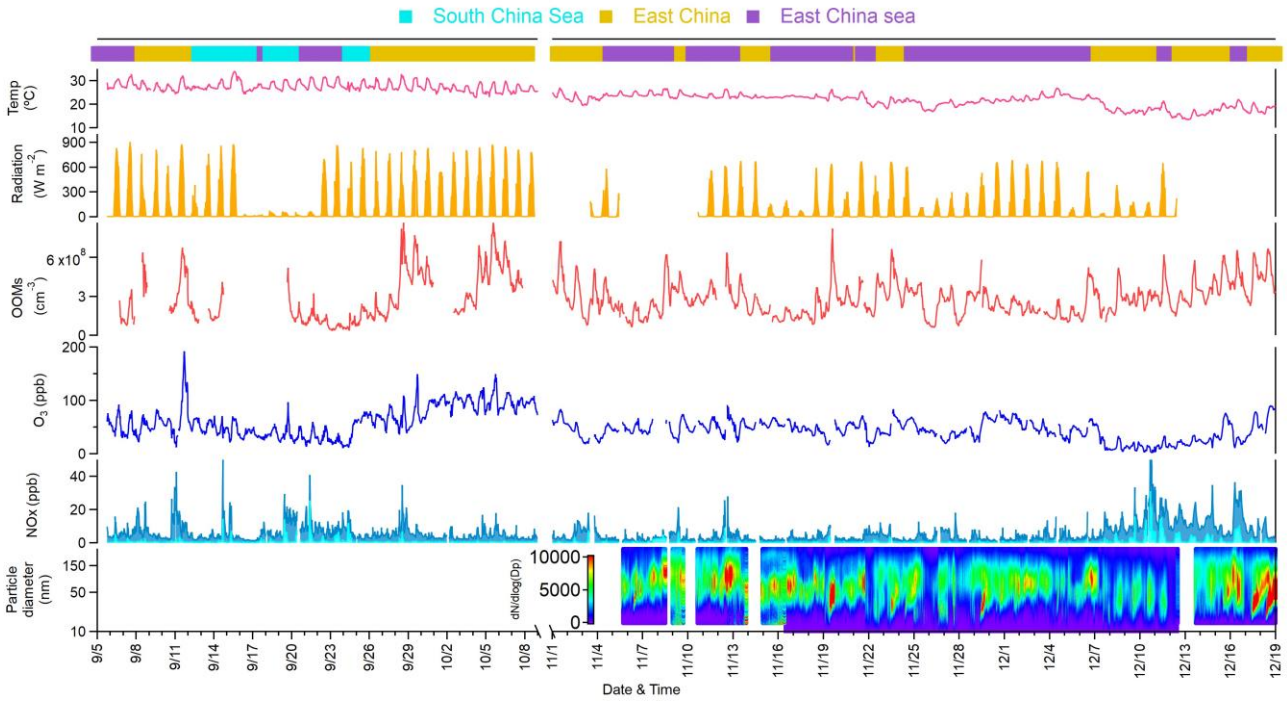

Figure S1 Time series of OOMs and related parameters including temperature, radiation, ozone, NOx and particle size distribution.

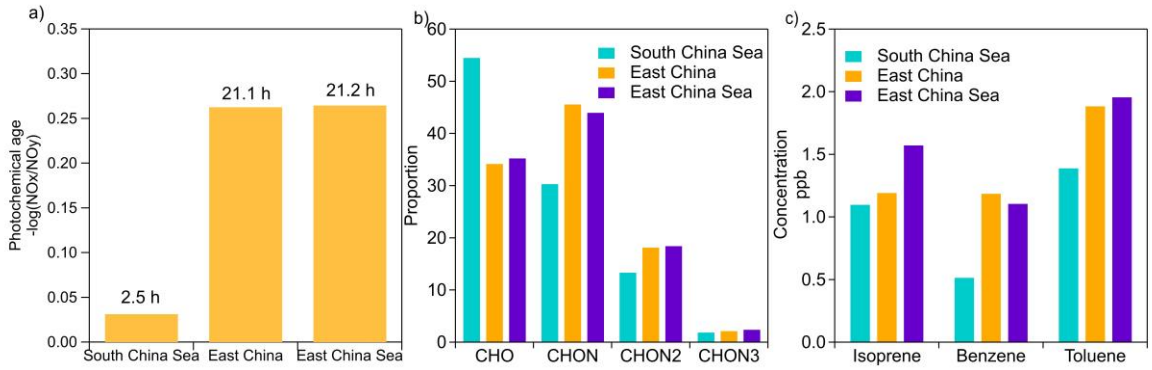

Figure S2 a) Photochemical ages of three clusters estimated with -log(NOx/NOy)[23]. b). The proportion comparison of CHO, CHON, CHON2, CHON3 OOMs in different clusters. c). The concentration of OOMs precursors in three clusters.

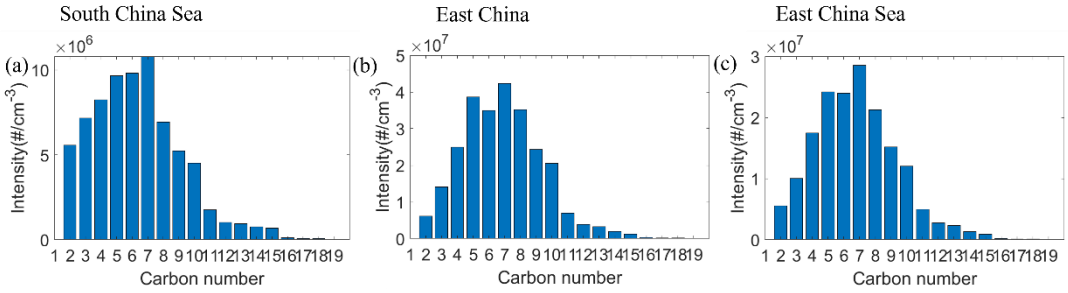

Figure S3 The carbon distribution of OOMs in three clusters.

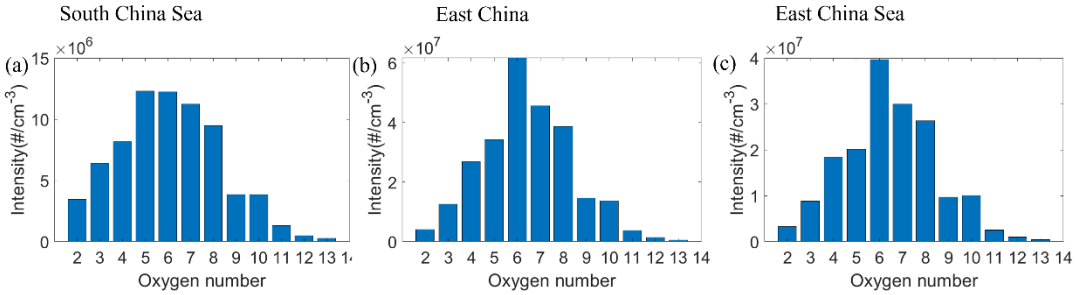

Figure S4 The oxygen distribution of OOMs in three clusters.

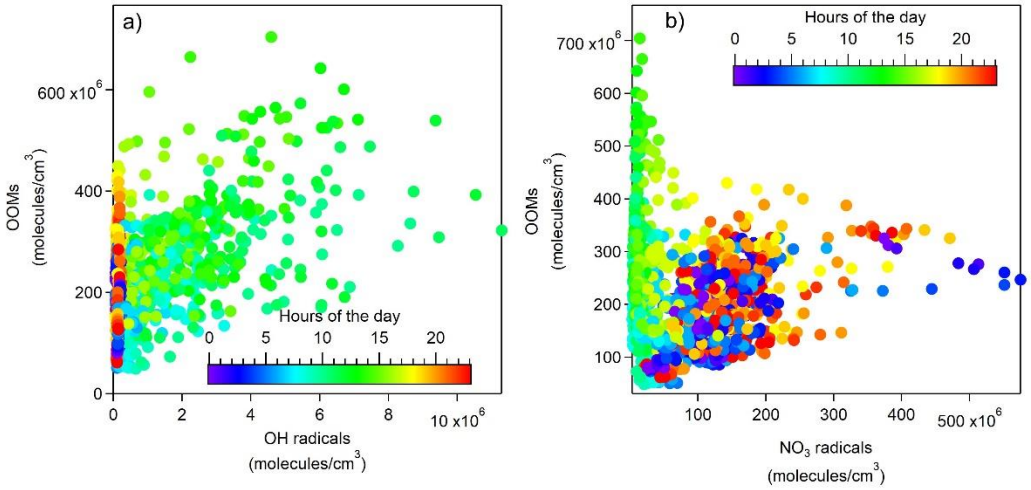

Figure S5 The correlation plot of OH, NO_3 radicals and OOMs

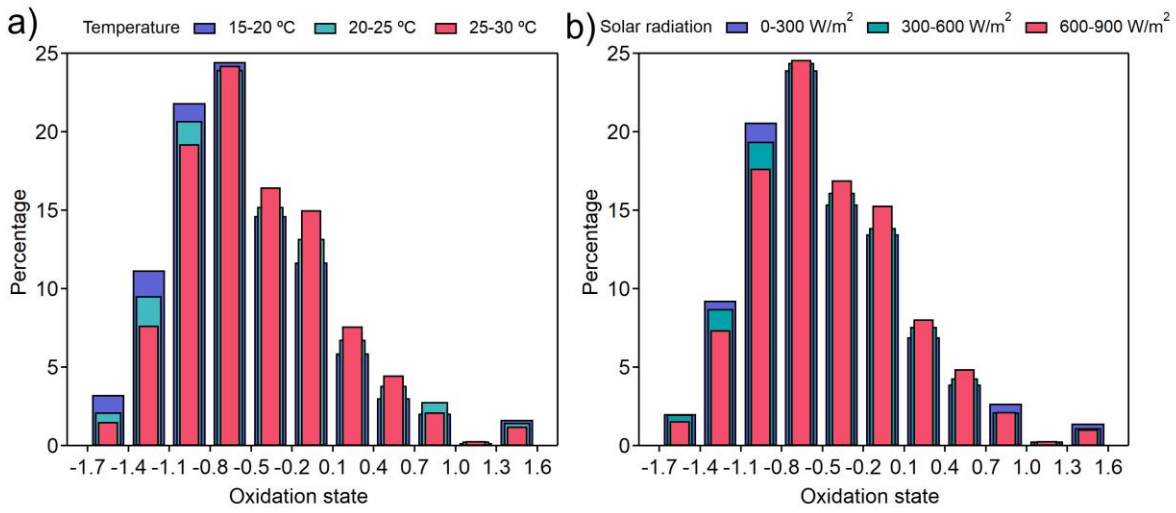

Figure S6 The OSc distribution of measured OOMs under different a) temperature and b) solar radiation conditions

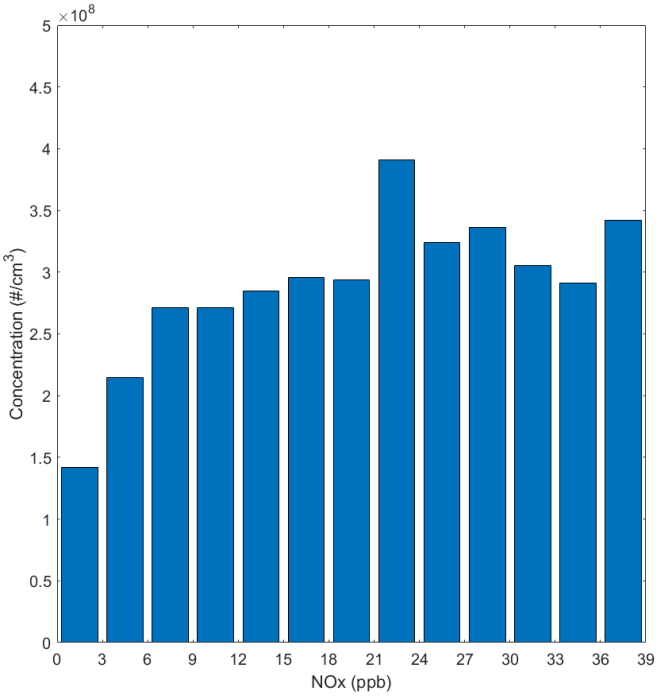

Figure S7 The OOMs concentration varied with NOx levels.

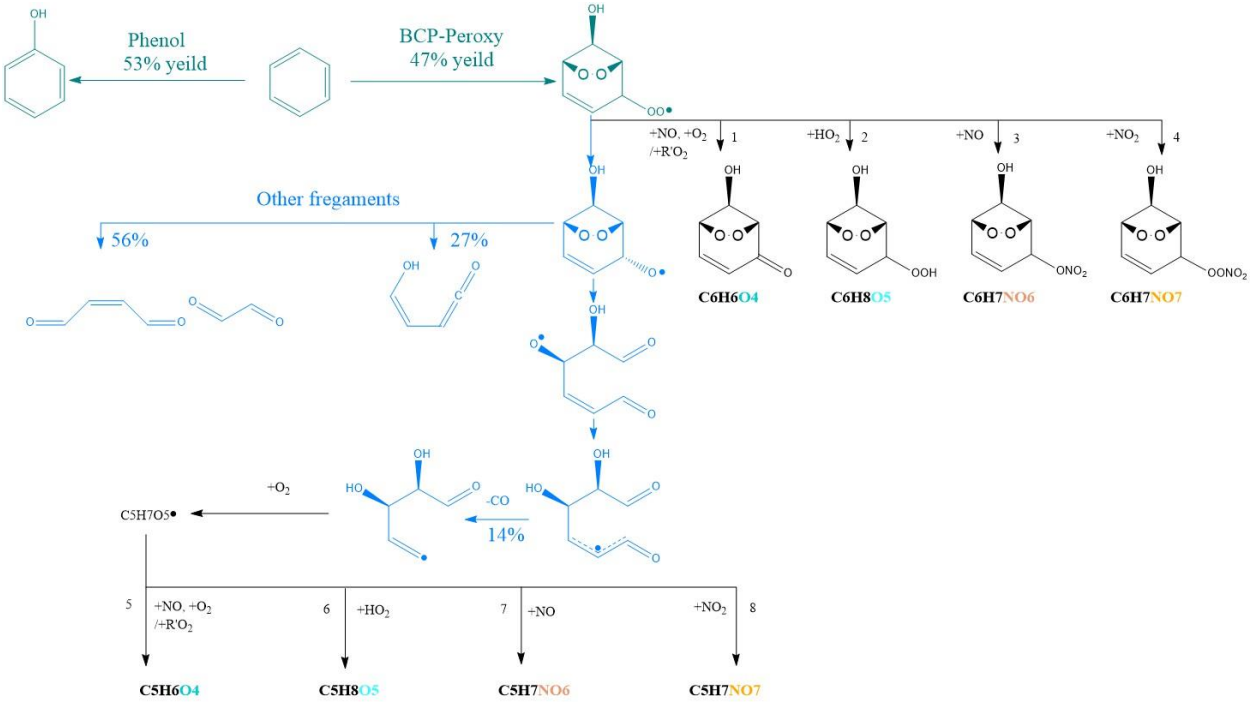

283

284 Figure S8 Chemical schematics of benzene oxidation by OH radicals.

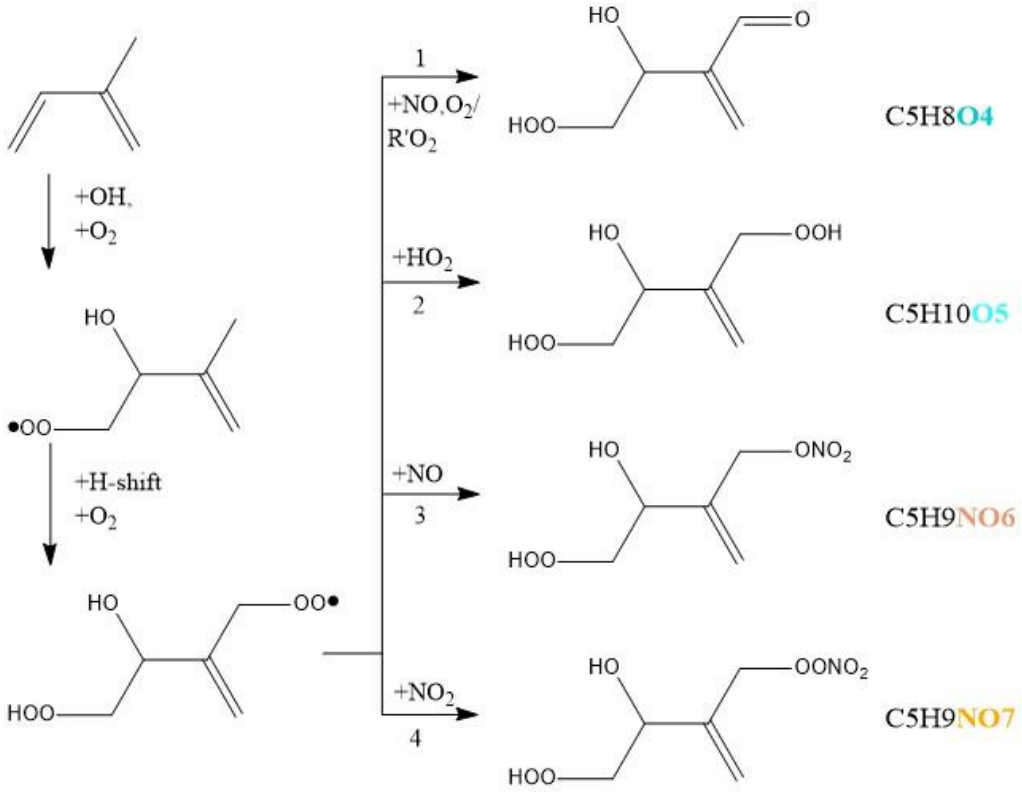

285

286 Figure S9 Chemical schematics of isoprene oxidation by OH radicals.

287

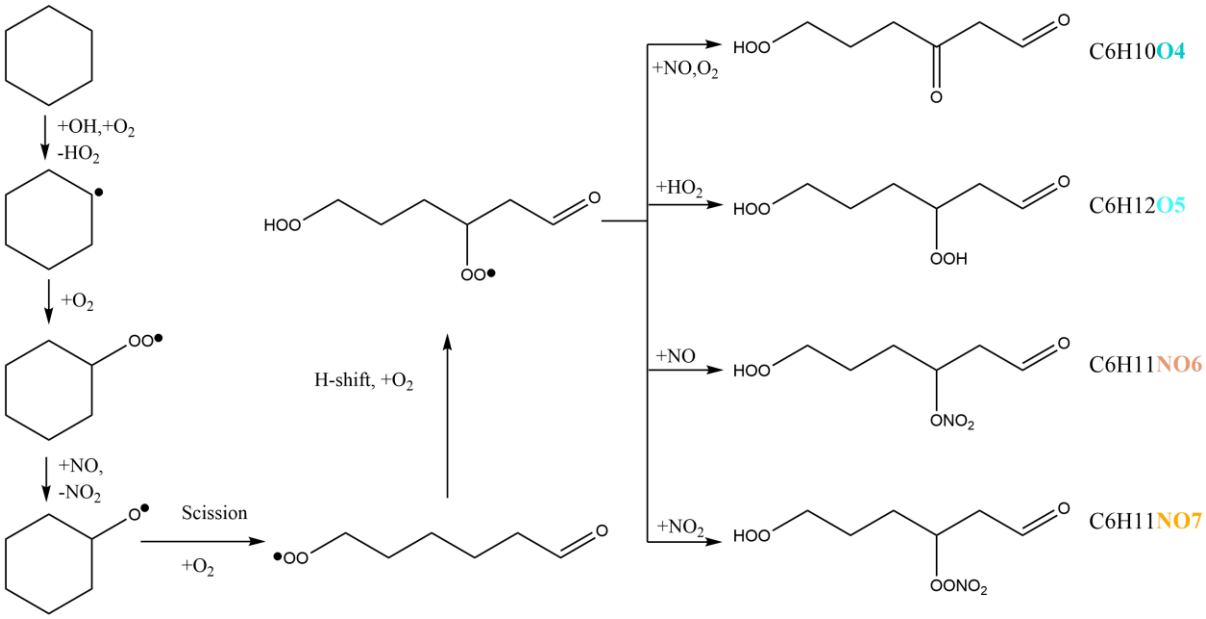

288

289 Figure S10 Chemical schematics of cyclohexane oxidation by OH radicals.

290

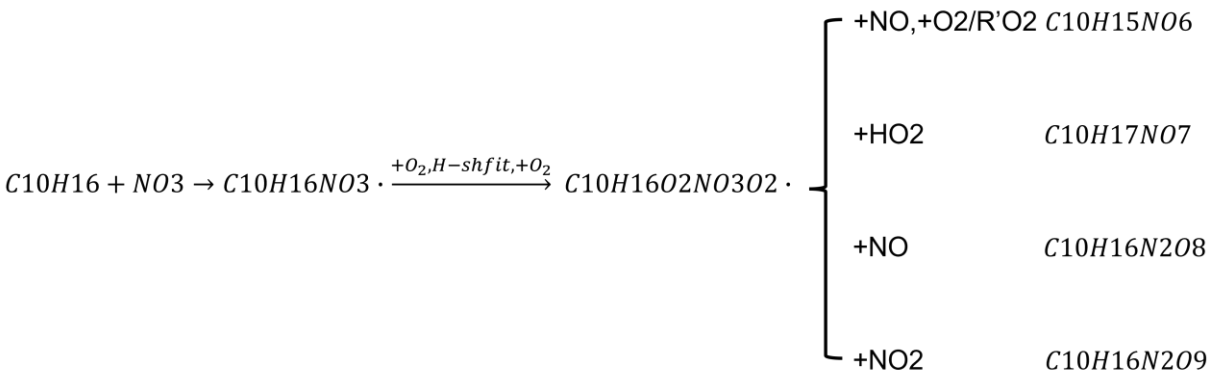

291

292 Figure S11 A simplified schematic of terpene oxidation mechanism by NO_3 radicals.

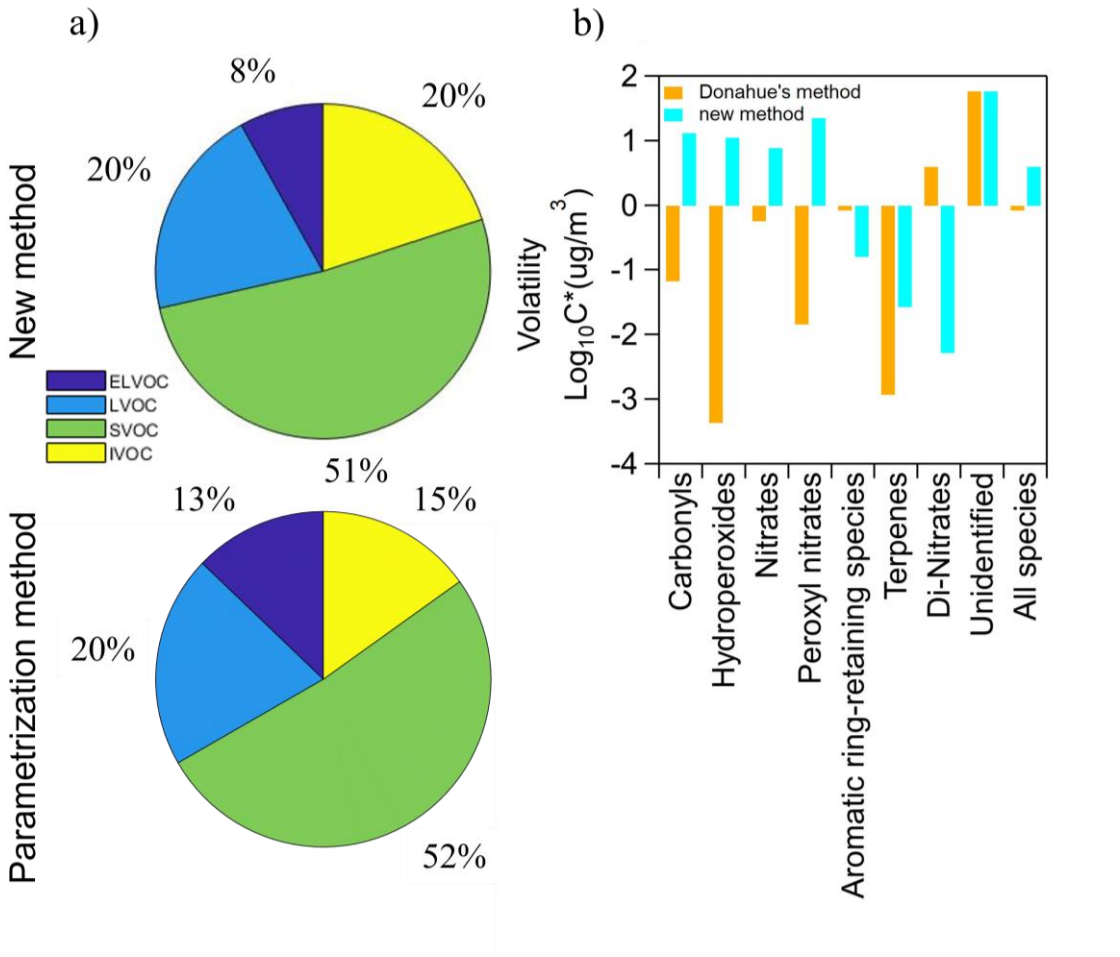

Figure S12 a) The comparison of ELVOC, LVOC, SVOC and IVOC distribution calculated with new method and parameterization methods. b) The comparison of species average volatility calculated with new method and parameterization methods, respectively.

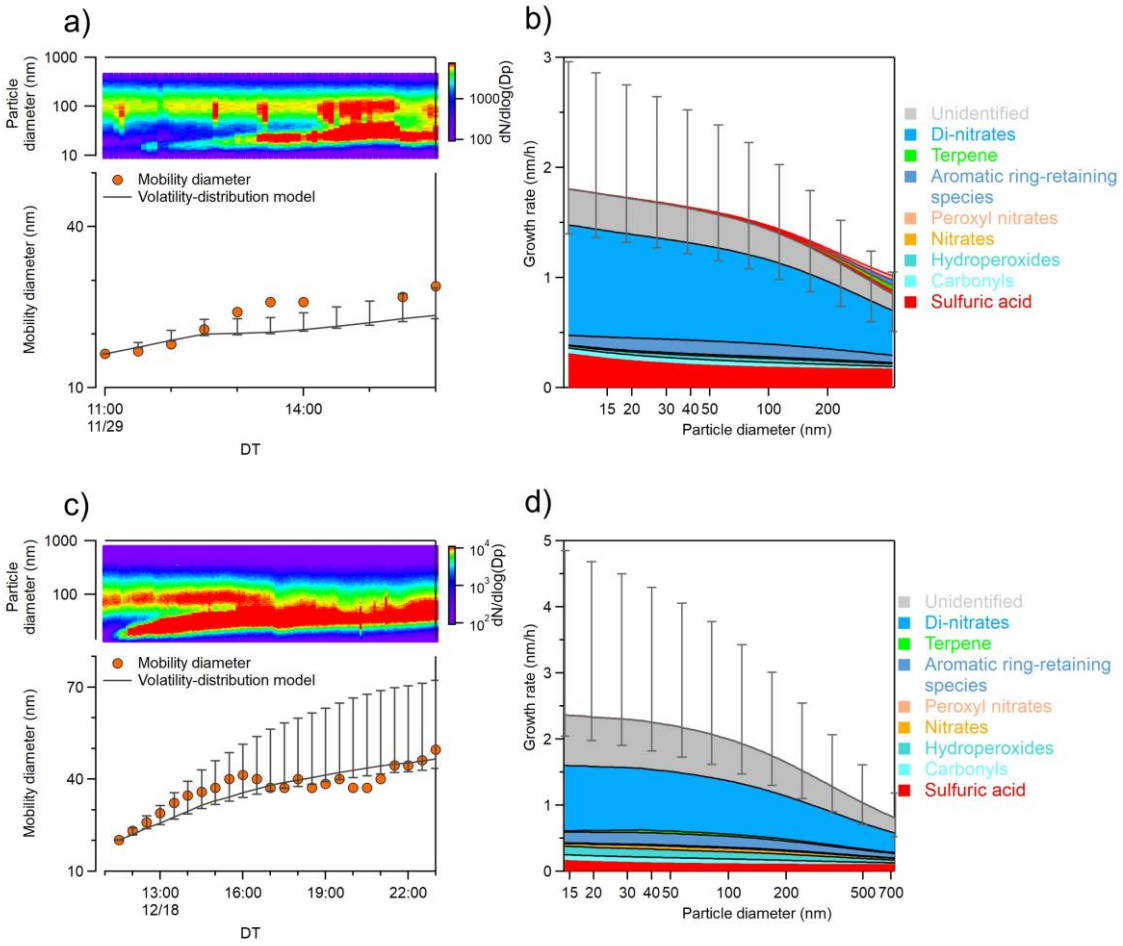

Figure S13 Another two particle formation and growth cases observed during the campaign, and were used to evaluate the OOMs contribution to the particle growth rate with new method. The labels and markers are the same in Figure 5. The OOMs contribution via equilibrium partitioning is insignificant, as shown by the red lines on top of the condensation contributions in Figure S13 b.

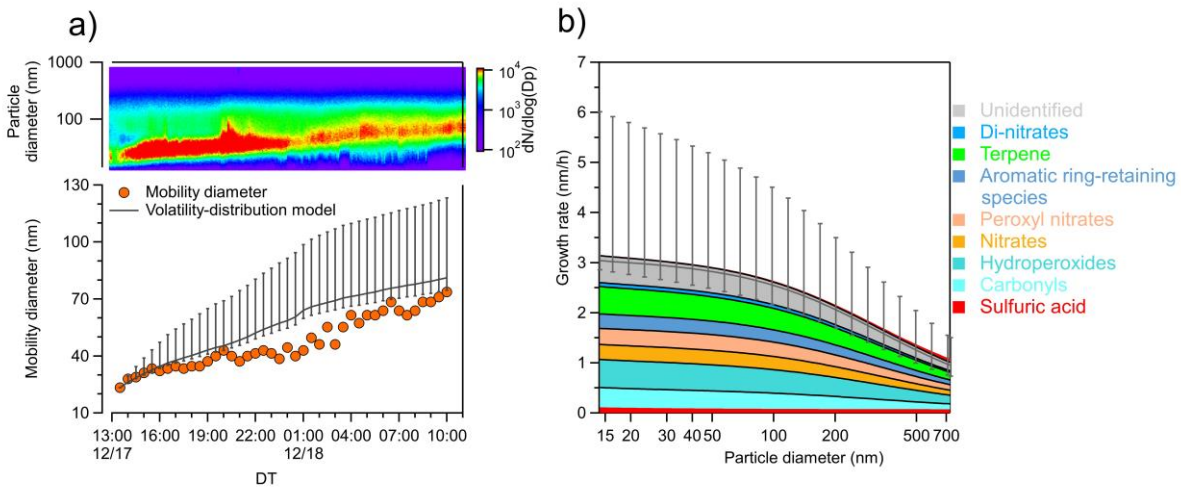

Figure S14 OOMs contribution to the particle growth in the same case in Figure 5, using volatility data estimated from the parameterization method. The labels and markers are the same in Figure 5.

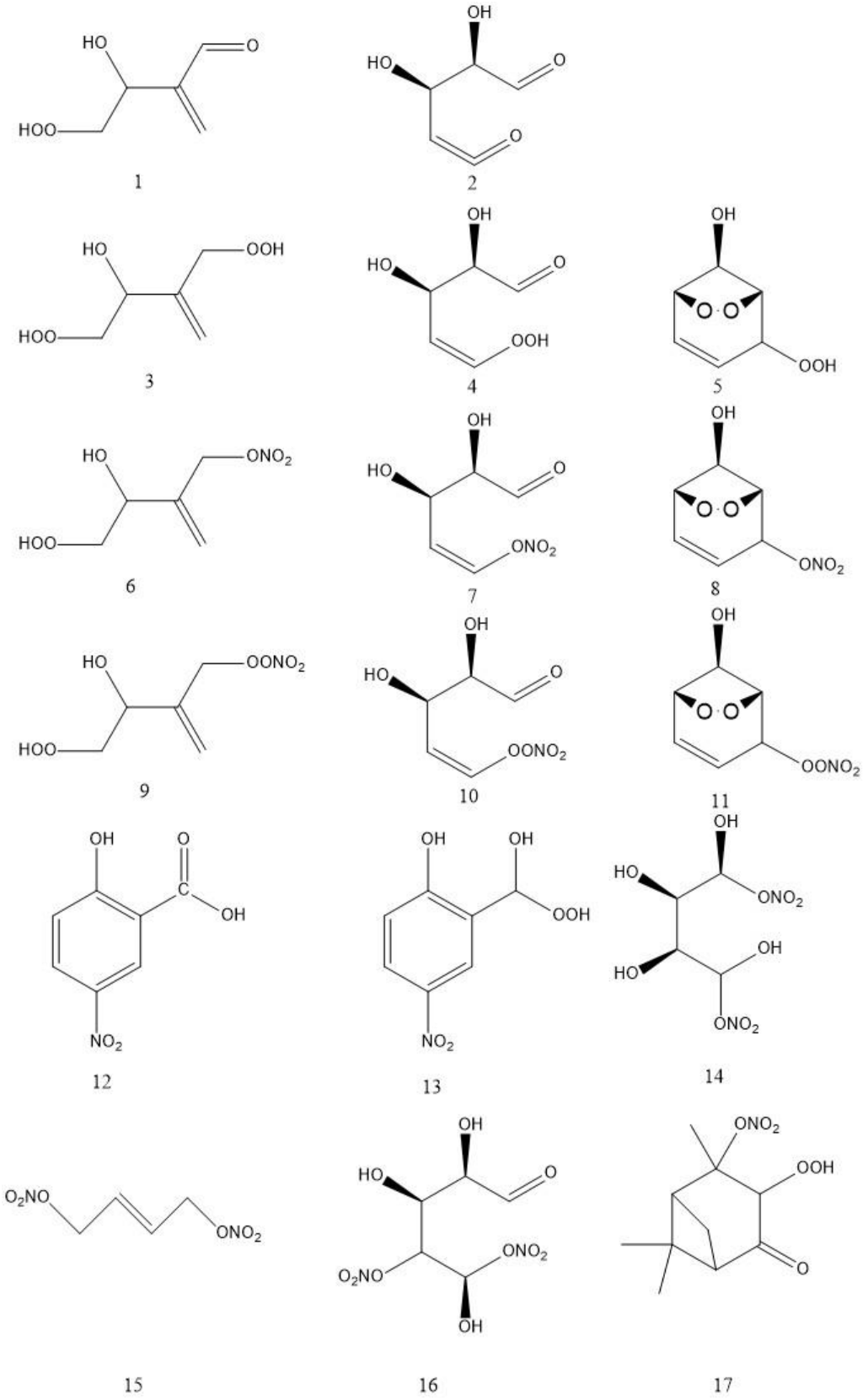

Figure S15 The examples of chemical structure of selected OOMs in Table S4

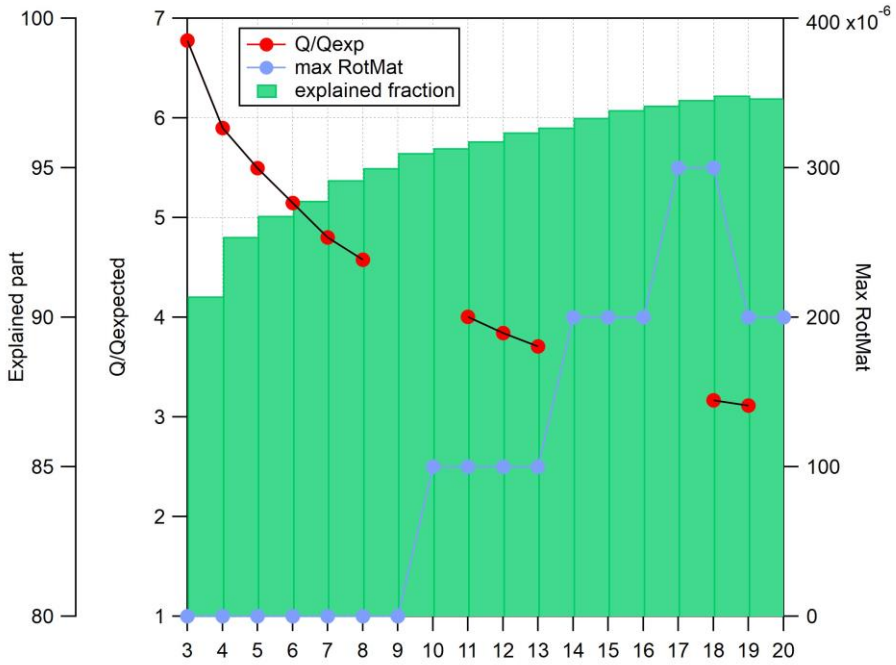

Figure S16 Mathematical diagnostics of PMF solutions, including values of Q/Qexp, the maximum value of rotation matrix (RotMat) versus the number of factors (Fpeak=0), and explained fraction of each solution.

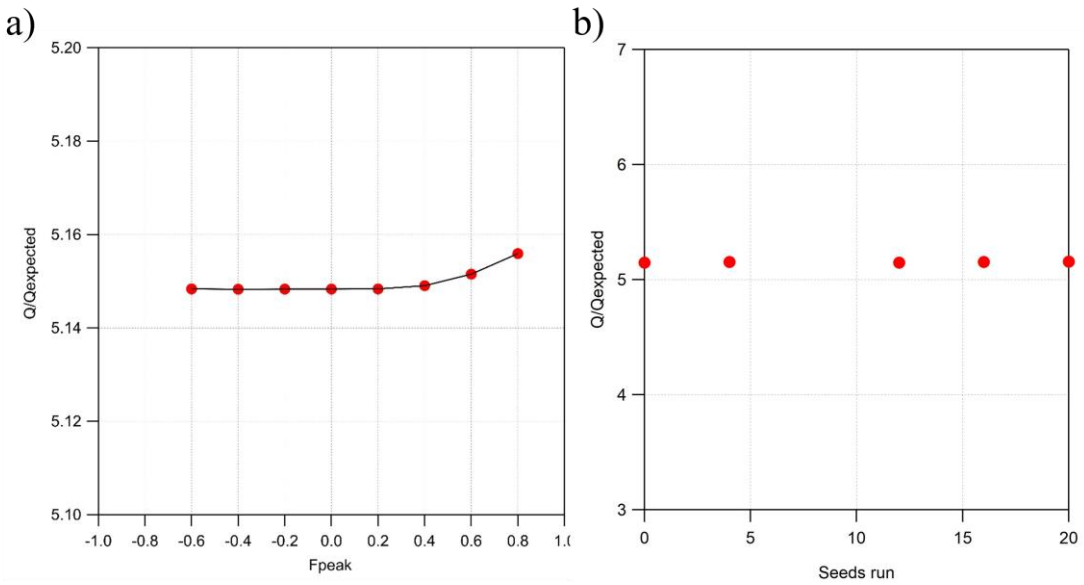

Figure S17 a) Values of Q/Qexp versus Fpeak for the six-factor solution. b) Five seeds run for the 6 factors solution.

Tables

Table S1 The mean temperature and theoretical global radiation of five sites

Sites	Period	OOMs concentration molecules/cm^3	Mean temperature °C	Mean theoretical global radiation[1] W/m^2
Hong Kong	Sep–Nov 2019	2.53×10^8	24.3	557
Shanghai	Nov-2018	7.80×10^7	13.9	485
Nanjing	Nov-2018	7.70×10^7	13.0	491
Beijing	Oct–Nov 2019	8.30×10^7	12.1	428
Beijing	Jul–Aug 2019	1.60×10^8	28.6	604

[1]Only daytime (7:00-17:00 LT) data was used to calculate the average theoretical global radiation of the sites.

Table S2 The metrics for OOMs classification

Categories	nC	nN	DBE	nO
Carbonyls	>=4, ≠10	0	2,3	4,6,8,10,12,14
Hydroperoxides	>=4, ≠10	0	1,2,3	5,7,9,11,13,15
Nitrates	>=4, ≠10	1	1,2,3	6,8,10,12,14,16
Peroxyl nitrates	>=4, ≠10	1	1,2,3	7,9,11,13,15,17
Aromatic ring-retaining species	>=6, ≠10	0,1	>=5	any
	>=6, ≠10	1	4	any
	>=6, ≠10	0	4	1,2,3
Terpene[1]	10	0,1,2	any	any
Di-nitrates	>=4, ≠10	2	any	any

[1]The OOMs with 10 C atoms was categorized as terpene-derived OOMs. Please be noted a small fraction of aliphatic and aromatic-derived OOMs may also be categorized as terpenes.

Table S3 The C10 terpene products reported in previous studies

Species	Concentration, molecules/m^3	Reference
C10H15O6N1	1495829	Shen et al. [24]
C10H18O8N2	1041096	Luo et al. [25]
C10H16O8N2	893120	Shen et al. [24]
C10H15O8N1	850181	Luo et al. [25]
C10H15O7N1	821767	Luo et al. [25]
C10H17O6N1	708587	Luo et al. [25]
C10H14O9	647231	Luo et al. [25]
C10H17O7N1	641890	Luo et al. [25]
C10H17O10N3	533552	Liu et al. [26]
C10H16O10N2	492237	Luo et al. [25]
C10H17O8N1	393955	Luo et al. [25]
C10H10O4	364370	
C10H19O6N1	339914	
C10H14O5	290387	Luo et al. [25]
C10H15O10N1	277571	Luo et al. [25]
C10H15O9N1	274790	Luo et al. [25]
C10H14O6	272431	Jokinen et al. [27]
C10H16O6	268858	Luo et al. [25]
C10H18O9N2	259964	Faxon et al. [28]
C10H16O5	253283	Luo et al. [25]
C10H14O9N2	225593	Luo et al. [25]
C10H17O9N1	219120	Luo et al. [25]
C10H16O8	202085	Luo et al. [25]
C10H20O7N2	187257	
C10H16O7N2	185693	Liu et al. [26]
C10H14O7	176416	Luo et al. [25]
C10H13O7N1	173264	Guo. et al. [29]
C10H17O11N3	159597	
C10H19O10N3	158415	
C10H18O10N2	148379	Luo et al. [25]
C10H17O10N1	147448	Luo et al. [25]
C10H14O10N2	142346	Luo et al. [25]
C10H16O4	140422	Guo. et al. [29]
C10H14O4	135858	Guo. et al. [29]
C10H15O10N3	135703	
C10H19O9N3	133602	
C10H19O8N1	133502	
C10H13O8N1	119191	Luo et al. [25]
C10H14O8N2	116364	Guo. et al. [29]
C10H18O6	99797	
C10H19O7N1	96796	
C10H18O7	85075	
C10H7O3N1	80477	

C10H18O6N2	78932	
C10H17O5N1	77922	Luo et al. [25]
C10H11O6N1	75652	
C10H11O8N1	73656	
C10H12O7	72570	
C10H16O11N2	70783	
C10H18O4	70485	Guo. et al. [29]
C10H12O9	66472	
C10H14O11N2	61214	Luo et al. [25]
C10H18O5	60121	Guo. et al. [29]
C10H19O9N1	56948	
C10H20O6	56391	
C10H13O6N1	50907	Guo. et al. [29]
C10H13O12N1	50887	
C10H13O5N1	50195	
C10H12O8	47553	
C10H18O11N2	46433	Luo et al. [25]
C10H16O13	46202	Luo et al. [25]
C10H19O11N1	43701	
C10H23O11N1	42618	
C10H21O6N1	42269	
C10H13O11N1	40695	Luo et al. [25]
C10H19O11N3	39446	
C10H12O9N2	34666	Guo. et al. [29]
C10H16O12N2	34598	
C10H16O7	33506	
C10H20O9N2	32525	
C10H22O11N2	31430	
C10H13O10N1	31314	
C10H14O13	30749	Luo et al. [25]
C10H11O7N1	29819	
C10H21O10N1	29505	
C10H10O10N2	28893	
C10H13O11N3	28844	
C10H21O10N3	28403	
C10H20O10N2	25356	
C10H9O10N1	25171	
C10H20O11	23315	
C10H19O12N1	22939	
C10H20O9N1	19203	
C10H13O10N3	18205	
C10H21O7N1	18027	
C10H20O8	17966	
C10H17O4N1	17848	
C10H9O11N1	9279	
C10H20O5	6466	

327

328 Table S4 The functional groups of classified OOMs in different categories

Species	DBE	nO	Functional groups (contribution to volatility)									Notes	Example
			C=O (-1)	C=C (-0.105)	-OH (-2.3)	-OOH (-2.3)	Non-aromatic ring (-0.0104)	Aromatic ring (-0.675)	-ONO2 (-2.5)	-OONO2 (-2.5)	-NO2 (-2.15)		
Carbonyls	2	any	1	1	1	1 + extra O/2	0	0	0	0	0	extra O only present in the -OOH group	1[1]
	3	any	2	1	2	extra O/2	0	0	0	0	0	extra O only present in the -OOH group	2
Hydroperoxides	1	any	0	1	1	2 + extra O/2	0	0	0	0	0	extra O only present in the -OOH group	3
	2	any	1	1	2	1 + extra O/2	0	0	0	0	0	extra O only present in the -OOH group	4
	3	any	0	1	1	1 + extra O/2	2	0	0	0	0	extra O only present in the -OOH group	5
Nitrates	1	any	0	1	1	1 + extra O/2	0	0	1	0	0	extra O only present in the -OOH group	6
	2	any	1	1	2	extra O/2	0	0	1	0	0	extra O only present in the -OOH group	7
	3	any	0	1	1	extra O/2	2	0	1	0	0	extra O only present in the -OOH group	8
Peroxyl nitrates	1	any	0	1	1	1 + extra O/2	0	0	0	1	0	extra O only present in the -OOH group	9
	2	any	1	1	2	extra O/2	0	0	0	1	0	extra O only present in the -OOH group	10
	3	any	0	1	1	extra O/2	2	0	0	1	0	extra O only present in the -OOH group	11
Aromatic ring-retaining species	=nC-2	any	1	0	1+ extra O/3	extra O/3	0	1	0	0	nN	extra O evenly distribute in the -OOH and -OH group	12
	>nC-2	any	0	DBE-4	1+ extra O/3	extra O/3	0	1	0	0	nN	extra O evenly distribute in the -OOH and -OH group	13

	0	any	0	0	extra O	0	0	0	2	0	0	extra O only present in the -OH group	14
Dinitrates	1,2,3	6	0	DBE	0	0	0	0	2	0	0		15
	1,2,3	>6	0	DBE-1	extra O	0	0	0	2	0	0	extra O only present in the -OH group	16
Terpenes	any	any										Tröstl et al.'s method	17
Unidentified	any	any										Parameterization methods	

[1]Examples are shown in Figure S15

330

331 Table S5 Peak list of nitrophenols, contamination, chloride, bromide, iodide and sulfide

Nitrophenols	Contaminations		Cl, Br, I, S containing species		
C6H5O3N1	C2H1O2F3	C7H4O3F12	H2O4S1	H1O6N1S1	C2H5O7Cl1
C7H7O3N1	C6H6O1N2F5	C2H3F3	C6H4O3N1Cl1	C2H2O1Br2	H2O9N2S1
C6H4O5N2	C3H1O2F5	C5H3F9	H1Cl1	C5H1O2N2Cl1Br1	C4H7O9N1S1
C7H6O5N2	C4H1O2F7	C6H2F12	H1O5S1	C2H1O2Cl3	C5H6O1Cl1Br1
C8H9O3N1	C5H2O2F8	C7H2O2F12	C2H2O2Cl2	C1H4O3S1	H4O8S2
C6H5O4N1	C3H4O3F4	C5H3O1F11	H1O4S1	C3H6O6Cl2	H2O8N1S1
C8H8O5N2	C5H1O2F9	C1H4O1F2	H3O1Cl1	H4O5S1	H1O5S2
C7H7O4N1	C4H2O4F6	C7H1O2F13	C6H3O3N1Cl2	C5H8Cl1Br1	C4H8O6Cl2
C9H11O3N1	C4H2O2F6	C2H4O1F4	H1O6N2I1	C4H1O4Cl1	H2O10N2S1
C8H9O4N1	C3H2O2F4	C6H3O1F13	C3H5O3Cl1	C3H1O3Cl1F2	C1O1S1
C9H9O3N1	C6H3F11	C2H3O1F5	C3H3O3Cl1	C1H1Cl3	H1O2N1S1
C6H4O6N2	C1H1F3	C3H3O3F5	C3H3O2Cl1	C6H6O4S2	
C7H5O3N1	C5H4O3F8	C2H2O2F2	C2H3O2Cl1	C6H7O7Cl1	
C9H11O4N1	C2H1O4F1		H2O6N1I1	C3H5O6N1Cl2	
C7H6O6N2	C4H4O4F4		H5O2Cl1	C3H5O6Cl1	
C10H13O3N1	C6H1O2F11		H1Br1	C4H7Cl3	
C6H6O7N2	C2H4O3F2		H1O3I1	C3H5O4Cl3	
C9H10O1	C3H1F7		H3O8S3	C4H2O3Cl2	
C7H8O7N2	C3H3F5		C4H5O4Cl1	C3H3O2Br1	
C7H7O8N3	C4H1F9		C3H4O2N1I1	C8H5O1Br1	
C6H5O5N1	C2H1F5		H1O7N1S1	C6H9O10Cl1	

332

333 Table S6 The evolution of PMF factors

Size of factor space																	
3		4		5		6		7		8		9	
Fr.[1]	Id.[2]	Fr.	Id.	Fr.	Id.	Fr.	Id.	Fr.	Id.	Fr.	Id.	Fr.	Id.
27.2	0N[3]	23.7	MT, iso mixed	15.0	0N	13.9	O5	13.7	O5	11.5	O5	12.9	O4, O5, 1N, 2N mixed
25.4	2N	19.5	0N	17.3	MT, iso mixed	15.9	O4	11.5	O4	13.0	O4,1N mixed	11.0	O4,1N mixed
38.1	1N	20.2	2N	20.9	2N	14.7	MT, iso mixed	15.6	NO6, 2N mixed	11.2	O4, NO6 mixed	10.1	O4,1N mixed
		29.2	1N	23.1	NO6	20.4	NO6	12.9	MT, iso mixed	11.3	O4, NO6, 2N mixed	11.9	1N, 2N mixed
				17.1	NO7	16.8	NO7	15.1	NO7, 2N mixed	12.3	MT, iso mixed	9.1	O4,1N mixed
						12.2	2N	14.1	NO6	12.9	NO6	9.7	MT, iso mixed
								11.6	NO6, 2N mixed	10.0	NO6, 2N mixed	8.9	NO7, 2N mixed
										12.9	NO7, 2N mixed	10.4	NO6, 2N mixed
												11.5	NO6, NO7 mixed
9.3	Residuals	7.3	Residuals	6.6	Residuals	6.1	Residuals	5.4	Residuals	5.0	Residuals	4.5	Residuals

334 [1]Fr. stands for the occupied fraction of the factors

335 [2]Id. stands for the identified name of the factors

336 [3]The factors are named with the atom numbers of carbon and nitrogen in the fingerprint peaks

References

(1) Junninen, H.; Ehn, M.; Petäjä, T.; Luosujärvi, L.; Kotiaho, T.; Kostiainen, R.; Rohner, U.; Gonin, M.; Fuhrer, K.; Kulmala, M.; et al. A high-resolution mass spectrometer to measure atmospheric ion composition. *Atmospheric Measurement Techniques* **2010**, *3* (4), 1039-1053. DOI: 10.5194/amt-3-1039-2010.

(2) Chen, Y.; Zheng, P.; Wang, Z.; Pu, W.; Tan, Y.; Yu, C.; Xia, M.; Wang, W.; Guo, J.; Huang, D.; et al. Secondary Formation and Impacts of Gaseous Nitro-Phenolic Compounds in the Continental Outflow Observed at a Background Site in South China. *Environmental science & technology* **2022**, *56* (11), 6933-6943. DOI: 10.1021/acs.est.1c04596.

(3) Nie, W.; Yan, C.; Huang, D. D.; Wang, Z.; Liu, Y.; Qiao, X.; Guo, Y.; Tian, L.; Zheng, P.; Xu, Z.; et al. Secondary organic aerosol formed by condensing anthropogenic vapours over China's megacities. *Nature Geoscience* **2022**, *15* (4), 255-261. DOI: 10.1038/s41561-022-00922-5.

(4) Kürten, A.; Rondo, L.; Ehrhart, S.; Curtius, J. Performance of a corona ion source for measurement of sulfuric acid by chemical ionization mass spectrometry. *Atmospheric Measurement Techniques* **2011**, *4* (3), 437-443. DOI: 10.5194/amt-4-437-2011.

(5) Kurten, A.; Rondo, L.; Ehrhart, S.; Curtius, J. Calibration of a chemical ionization mass spectrometer for the measurement of gaseous sulfuric acid. *The journal of physical chemistry. A* **2012**, *116* (24), 6375-6386. DOI: 10.1021/jp212123n.

(6) Heinritzi, M.; Simon, M.; Steiner, G.; Wagner, A. C.; Kurten, A.; Hansel, A.; Curtius, J. Characterization of the mass-dependent transmission efficiency of a CIMS. *Atmospheric Measurement Techniques* **2016**, *9* (4), 1449-1460. DOI: 10.5194/amt-9-1449-2016.

(7) Paatero, P.; Tapper, U. Analysis of Different Modes of Factor-Analysis as Least-Squares Fit Problems. *Chemometrics and Intelligent Laboratory Systems* **1993**, *18* (2), 183-194. DOI: Doi 10.1016/0169-7439(93)80055-M.

(8) Yan, C.; Nie, W.; Aijala, M.; Rissanen, M. P.; Canagaratna, M. R.; Massoli, P.; Junninen, H.; Jokinen, T.; Sarnela, N.; Hame, S. A. K.; et al. Source characterization of highly oxidized multifunctional compounds in a boreal forest environment using positive matrix factorization. *Atmospheric Chemistry and Physics* **2016**, *16* (19), 12715-12731, Article. DOI: 10.5194/acp-16-12715-2016.

(9) Ulbrich, I. M.; Canagaratna, M. R.; Zhang, Q.; Worsnop, D. R.; Jimenez, J. L. Interpretation of organic components from Positive Matrix Factorization of aerosol mass spectrometric data. *Atmospheric Chemistry and Physics* **2009**, *9* (9), 2891-2918. DOI: 10.5194/acp-9-2891-2009.

(10) Paatero, P.; Hopke, P. K.; Song, X. H.; Ramadan, Z. Understanding and controlling rotations in factor analytic models. *Chemometrics and Intelligent Laboratory Systems* **2002**, *60* (1-2), 253-264. DOI: Doi 10.1016/S0169-7439(01)00200-3.

(11) Lee, E.; Chan, C. K.; Paatero, P. Application of positive matrix factorization in source apportionment of particulate pollutants in Hong Kong. *Atmospheric Environment* **1999**, *33* (19), 3201-3212. DOI: Doi 10.1016/S1352-2310(99)00113-2. Lanz, V. A.; Alfarra, M. R.; Baltensperger, U.; Buchmann, B.; Hueglin, C.; Prevot, A. S. H. Source apportionment of submicron organic aerosols at an urban site by factor analytical modelling of aerosol mass spectra. *Atmospheric Chemistry and Physics* **2007**, *7* (6), 1503-1522. DOI: DOI 10.5194/acp-7-1503-2007.

(12) Reff, A.; Eberly, S. I.; Bhave, P. V. Receptor modeling of ambient particulate matter data using positive matrix factorization: review of existing methods. *J Air Waste Manag Assoc* **2007**, *57* (2), 146-154. DOI: 10.1080/10473289.2007.10465319.

(13) Donahue, N. M.; Epstein, S. A.; Pandis, S. N.; Robinson, A. L. A two-dimensional volatility basis set: 1. organic-aerosol mixing thermodynamics. *Atmospheric Chemistry and*

Physics **2011**, *11* (7), 3303-3318. DOI: 10.5194/acp-11-3303-2011.
(14) Trostl, J.; Chuang, W. K.; Gordon, H.; Heinritzi, M.; Yan, C.; Molteni, U.; Ahlm, L.; Frege, C.; Bianchi, F.; Wagner, R.; et al. The role of low-volatility organic compounds in initial particle growth in the atmosphere. *Nature* **2016**, *533* (7604), 527-531. DOI: 10.1038/nature18271.
(15) Ehn, M.; Thornton, J. A.; Kleist, E.; Sipila, M.; Junninen, H.; Pullinen, I.; Springer, M.; Rubach, F.; Tillmann, R.; Lee, B.; et al. A large source of low-volatility secondary organic aerosol. *Nature* **2014**, *506* (7489), 476-479. DOI: 10.1038/nature13032. Stolzenburg, D.; Fischer, L.; Vogel, A. L.; Heinritzi, M.; Schervish, M.; Simon, M.; Wagner, A. C.; Dada, L.; Ahonen, L. R.; Amorim, A.; et al. Rapid growth of organic aerosol nanoparticles over a wide tropospheric temperature range. *Proceedings of the National Academy of Sciences of the United States of America* **2018**, *115* (37), 9122-9127. DOI: 10.1073/pnas.1807604115.
(16) Mohr, C.; Thornton, J. A.; Heitto, A.; Lopez-Hilfiker, F. D.; Lutz, A.; Riipinen, I.; Hong, J.; Donahue, N. M.; Hallquist, M.; Petaja, T.; et al. Molecular identification of organic vapors driving atmospheric nanoparticle growth. *Nature communications* **2019**, *10* (1), 4442. DOI: 10.1038/s41467-019-12473-2.
(17) Pankow, J. F.; Asher, W. E. SIMPOL.1: a simple group contribution method for predicting vapor pressures and enthalpies of vaporization of multifunctional organic compounds. *Atmospheric Chemistry and Physics* **2008**, *8* (10), 2773-2796. DOI: DOI 10.5194/acp-8-2773-2008.
(18) Donahue, N. M.; Robinson, A. L.; Stanier, C. O.; Pandis, S. N. Coupled partitioning, dilution, and chemical aging of semivolatile organics. *Environmental science & technology* **2006**, *40* (8), 2635-2643. DOI: 10.1021/es052297c.
(19) Stolzenburg, D.; Simon, M.; Ranjithkumar, A.; Kürten, A.; Lehtipalo, K.; Gordon, H.; Nieminen, T.; Pichelstorfer, L.; He, X.-C.; Brilke, S.; et al. Enhanced growth rate of atmospheric particles from sulfuric acid. *ACP* **2019**. DOI: 10.5194/acp-2019-755.
(20) Seinfeld, J. H. *Atmospheric chemistry and physics : from air pollution to climate change*; Hoboken, New Jersey : Wiley, 2016.
(21) Ding, A.; Wang, T.; Fu, C. Transport characteristics and origins of carbon monoxide and ozone in Hong Kong, South China. *Journal of Geophysical Research: Atmospheres* **2013**, *118* (16), 9475-9488. DOI: 10.1002/jgrd.50714.
(22) Stohl, A.; Forster, C.; Eckhardt, S.; Spichtinger, N.; Huntrieser, H.; Heland, J.; Schlager, H.; Wilhelm, S.; Arnold, F.; Cooper, O. A backward modeling study of intercontinental pollution transport using aircraft measurements. **2003**, *108* (D12). DOI: https://doi.org/10.1029/2002JD002862.
(23) Zhou, S.; Wang, T.; Wang, Z.; Li, W.; Xu, Z.; Wang, X.; Yuan, C.; Poon, C. N.; Louie, P. K. K.; Luk, C. W. Y.; et al. Photochemical evolution of organic aerosols observed in urban plumes from Hong Kong and the Pearl River Delta of China. *Atmospheric Environment* **2014**, *88*, 219-229. DOI: 10.1016/j.atmosenv.2014.01.032.
(24) Shen, H.; Zhao, D.; Pullinen, I.; Kang, S.; Vereecken, L.; Fuchs, H.; Acir, I. H.; Tillmann, R.; Rohrer, F.; Wildt, J.; et al. Highly Oxygenated Organic Nitrates Formed from NO(3) Radical-Initiated Oxidation of beta-Pinene. *Environmental science & technology* **2021**, *55* (23), 15658-15671. DOI: 10.1021/acs.est.1c03978.
(25) Luo, H.; Vereecken, L.; Shen, H.; Kang, S.; Pullinen, I.; Hallquist, M.; Fuchs, H.; Wahner, A.; Kiendler-Scharr, A.; Mentel, T. F.; et al. Formation of highly oxygenated organic molecules from the oxidation of limonene by OH radical: significant contribution of H-abstraction pathway. *Atmos. Chem. Phys. Discuss.* **2022**, *2022*, 1-23. DOI: 10.5194/acp-2022-803.
(26) Liu, Y. L.; Nie, W.; Li, Y. Y.; Ge, D. F.; Liu, C.; Xu, Z. N.; Chen, L. D.; Wang, T. Y.; Wang,

L.; Sun, P.; et al. Formation of condensable organic vapors from anthropogenic and biogenic volatile organic compounds (VOCs) is strongly perturbed by NOx in eastern China. *Atmospheric Chemistry and Physics* **2021**, *21* (19), 14789-14814. DOI: 10.5194/acp-21-14789-2021.
(27) Jokinen, T.; Berndt, T.; Makkonen, R.; Kerminen, V. M.; Junninen, H.; Paasonen, P.; Stratmann, F.; Herrmann, H.; Guenther, A. B.; Worsnop, D. R.; et al. Production of extremely low volatile organic compounds from biogenic emissions: Measured yields and atmospheric implications. *Proceedings of the National Academy of Sciences of the United States of America* **2015**, *112* (23), 7123-7128. DOI: 10.1073/pnas.1423977112.
(28) Faxon, C.; Hammes, J.; Le Breton, M.; Pathak, R. K.; Hallquist, M. Characterization of organic nitrate constituents of secondary organic aerosol (SOA) from nitrate-radical-initiated oxidation of limonene using high-resolution chemical ionization mass spectrometry. *Atmospheric Chemistry and Physics* **2018**, *18* (8), 5467-5481. DOI: 10.5194/acp-18-5467-2018.
(29) Guo, Y. S.; Yan, C.; Liu, Y. L.; Qiao, X. H.; Zheng, F. X.; Zhang, Y.; Zhou, Y.; Li, C.; Fan, X. L.; Lin, Z. H.; et al. Seasonal variation in oxygenated organic molecules in urban Beijing and their contribution to secondary organic aerosol. *Atmospheric Chemistry and Physics* **2022**, *22* (15), 10077-10097. DOI: 10.5194/acp-22-10077-2022.